Hindawi
Indoor Air
Volume 2023, Article ID 5522169, 24 pages
https://doi.org/10.1155/2023/5522169

Research Article

Airborne Pollutant Removal Effectiveness and Hidden Pollutant Source Identification of Bionic Ventilation Systems: Direct and Inverse CFD Demonstrations

Hong-Liang Zhang,[1] Bin Li,[1] Jin Shang,[1] Wei-Wei Wang,[1] and Fu-Yun Zhao[1,2]

[1]*School of Power and Mechanical Engineering, Wuhan University, Wuhan, Hubei Province, China*
[2]*School of Civil Engineering, Hunan University of Technology, Zhuzhou, Hunan Province, China*

Correspondence should be addressed to Fu-Yun Zhao; zhao@bv.tum.de

Received 11 May 2023; Revised 21 October 2023; Accepted 25 November 2023; Published 16 December 2023

Academic Editor: Geun Young Yun

A healthy and efficient ventilation system is essential for establishing a comfortable indoor environment and significantly reducing a building's energy demand simultaneously. This paper proposed a novel ventilation system and applied it to the IEA Annex 20 mixing ventilation enclosure to verify its feasibility through mathematical modeling and CFD simulations. First, two bionic ventilation systems, single-side and dual-side ventilations, were compared to a conventional constant-volume supply system using CFD simulations, with the results demonstrating that the bionic ventilation system could provide higher ventilation efficiency and more effective pollutant removal from stagnant regions. Furthermore, the present work exercised these two bionic ventilation systems with different temporal periods of sine and rectangular wave functions, identifying a turning point at a period of 0.06 τ_n, which could contribute to further enhancement of these bionic ventilation systems. Finally, a methodology depending on the Bayesian inference algorithm was developed for identifying pollution sources in the bionic ventilation system with unstable flow fields, and factors influencing source identification accuracy were discussed. The results show that the peaks of the KDE distributions and the sampling average values of both the source location and intensity are all consistent with the actual source parameters. The potential of the proposed bionic ventilation systems has been well demonstrated by direct and inverse CFD models, paving the way for further engineering applications.

1. Introduction

Indoor air safety and health are complex and critical problems that pose a significant threat to billions of people's well-being. According to the Global Burden of Disease (GBD) 2019 study, air pollution (including outdoor fine particulate matter, ozone pollution, and indoor fine particulate matter pollution from fossil fuel combustion) was responsible for 6.6 million premature deaths globally, accounting for 11% of total deaths and ranking as the fourth leading risk factor for all disease burdens [1]. As people spend 80-90% of their time indoors, the majority of air pollution exposure occurs within indoor environments, incorporating both indoor and outdoor sources [2, 3]. Therefore, investigating indoor air pollution transport and control holds significant importance for safeguarding public health and minimizing social and economic losses [4].

Improving indoor air quality and ventilation efficiency is essential research that is aimed at enhancing the health and well-being of billions of individuals. Currently, there are two primary research approaches: one involves using inverse optimization methods to obtain optimal design parameters and ventilation strategies, while the other proposes new ventilation systems with innovative characteristics. The reverse optimization algorithm is based on the objective function to constraint to find the optimal solution, whose core idea is to calculate the input parameter values in reverse order from the objective output, such that the objective function is optimized. In ventilation system design, the reverse optimization algorithm can be used to determine the optimal

design parameters and ventilation strategies. Common inverse methods include CFD-based adjoint method, CFD-based genetic method, CFD-based artificial neural network method, and proper orthogonal decomposition method [5]. However, these methods only improve existing ventilation systems' performance, without addressing inherent flaws and limitations. Novel ventilation systems, such as displacement ventilation [6], impinging jet [7, 8], stratum ventilation [9, 10], and personalized ventilation [11, 12], are aimed at overcoming these issues.

Existing ventilation designs are based on the premise of constant supply parameters, including velocity and temperature. However, improvements achieved through reverse optimization design are limited by the presence of stagnant zones where pollutants accumulate under this premise. From a biomimetic perspective, ventilation systems share similarities with human or animal respiratory systems, both of which involve inhaling oxygen and exhaling carbon dioxide [13]. Studies have shown that the ventilation of buildings, human lungs, and even bird lungs are primarily convective fluid flows [14]. However, unlike these natural systems, which cyclically inhale and exhale air through the same "pipe system," built environment ventilation systems supply air at a constant velocity through independent supply and exhaust ducts [12]. Consequently, creating bionic ventilation systems with time-periodic conditions is an innovative and reasonable way to enhancing ventilation performance.

The available literature on room ventilation under time-periodic conditions appears to be quite limited. Kandzia et al. investigated the impact of a time-related variation in inlet velocity, at a scale of minutes, on the airflow characteristics in a room [15]. Their findings revealed that the stagnation zones, which were evident under steady conditions with a constant supply velocity, were absent in the time-average velocity field under unsteady cases. Another study by Sattari et al. found that pulsating inlet conditions resulted in an amplification of the distribution and intensity of vortices, accompanied by a decrease in stagnation zones [16]. Both of these phenomena contributed to an improvement in the air mixing within the room. Van Hooff and Blocken studied the mixing ventilation derived by two oppositely supply jets with a time-periodic (sine function) supply velocity, finding that it can reduce high pollutant concentration in stagnant regions and reduce the overall time-averaged pollutant concentration [17]. In summary, several studies have demonstrated the potential benefits of time-varying air supply conditions, but further research is needed to fully comprehend their advantages and limitations. This paper proposes two periodic supply methods to generate a more uniform time-averaged velocity distribution, reduce the stagnant zones of pollutants, and achieve higher ventilation efficiency. The present study is distinguished from prior research in that it employs a time-varying supply flow rate, rather than a constant supply. Additionally, the study distinguishes itself from situations where variable-air-volume (VAV) ventilation [18], demand-controlled ventilation [19], or specific ventilation schedules [20] are utilized, as these scenarios typically involve relatively large time scales, such as one hour, resulting in the persistence of a statistically stationary flow pattern within the room. This paper focuses on relatively small-time scales and their influence on indoor airflow distribution and is aimed at improving ventilation efficiency by enhancing the mixing of room air with fresh supply air, achieved through the breakdown of stagnation regions.

The identification of indoor pollution sources' positional parameters is mainly achieved through sensor data that tracks pollution source information, a task that belongs to the domain of inverse problems [21–24]. The methods used in this process can be categorized into four groups: (1) direct methods based on regularization or stabilization methods, (2) traditional probability methods based on Bayesian inference or joint probability methods coupled with transport processes, (3) optimization methods based on gradient or heuristic algorithms, and (4) analytical methods combining regularization techniques for inference.

Among them, probability-based and optimization-based methods have gained widespread attention and development [25]. The essential difference between them lies in the use of probability in the former, which considers input and output uncertainties in the inverse model, representing the solution as a probability distribution with a certain confidence interval using Bayesian principles, while the latter seeks a single extremum.

Accurately locating pollution sources in the bionic ventilation system proposed in this paper is particularly challenging due to the complexity of the supply system, especially when attempting to identify pollution sources within dynamic flow fields. This paper first investigated the mechanism of unsteady flow fields and nonlinear pollutant propagation underlying time-periodic supply velocity creation. Bayesian inference was then employed to develop a methodology for identifying pollution sources in indoor environments under dynamic flow fields and discussion. The factors influencing the accuracy of source identification were discussed in detail.

This paper is organized as follows. In Section 2, Bayesian inference and the source-receptor relationships under dynamic indoor flow fields were established. In Section 3, the computational methodology and simulation parameters were described and validated using experimental data in Section 4. Finally, the characteristic analysis of the bionic ventilation system and source term estimation results are drawn in Section 5. Section 6 concludes the work presented.

2. Methodology for Source Identifications: Inverse CFD Models

In this paper, the characteristics of bionic ventilation systems were analyzed through CFD numerical simulations. Furthermore, Bayesian inference for source identification in the dynamic indoor environment is further developed by considering time-periodic air supply, which is suitable for the bionic ventilation system.

2.1. Bayesian Inference. The Bayesian theorem is employed to determine the possibility of an event occurring conditional on another event, as Equation (1). Different from traditional statistical inference, Bayesian inference preserves uncertainty and believes that probability represents the

degree of the credibility [26]. It builds on existing knowledge of events.

$$p(M|D,I) = \frac{p(M|I)p(D|M,I)}{P(D|I)}. \quad (1)$$

For the inverse problem of pollutant identification in indoor environments, M represents the pollutant model parameters, D denotes the observation data of various detectors, I signifies the available model and related information. $p(M|I)$ is the prior probability density function (PDF) for substituting random variable parameters, typically derived from prior expert experience or direct assumptions. $p(D|M,I)$ represents the likelihood that the model results fit the observed data when the model parameters (M) are determined. $p(M|D,I)$ is the posterior PDF, namely, the result of estimation. When Bayesian inference is applied to identify unknown pollution sources in indoor environments, the PDF of model parameter M is updated by obtaining observed data D continuously.

In Equation (1), the denominator $p(D|I)$ is the marginal likelihood function, representing the applicability of the model M when the obsessed data D is obtained. This marginal likelihood function is expressed as $\int p(M|I)p(D|M,I)dM$, which is often as an integral constant. In high-dimensional problems, this integral is different to solve and is typically normalized for simplification. Generally, this process does not affect the parameters optimization for a single model system [27]. In this paper, source term identification is a single model system only considering the pollutant transport equation, and the Bayesian inference is expressed as Equation (2).

$$p(M|D,I) \propto p(M|I)p(D|M,I). \quad (2)$$

The prior distribution $p(M|I)$ is independent of the observed data D. Commonly used prior distributions include uniform distribution, Gaussian normal distribution, mixed distribution, and pulse distribution [28]. Uniform distribution is often an effective choice when only the upper and lower limits of parameters are known. The focus is more on the sensitivity of the posterior distribution to the prior, rather than the exact expression. In this paper, source term estimation based on the pollutant advection-diffusion equation is not sensitive to the form of the prior distribution.

2.2. Likelihood Function. The likelihood function $p(D|M,I)$ represents the likelihood between the output values from models and the detection values from detectors and is expressed as a PDF. An appropriate likelihood function has a significant impact on estimating source terms accurately, stably, and quickly and is a critical aspect of constructing Bayesian inference models. In this paper, the observation error is incorporated and independent of the system. The mathematical system can be expressed as follows:

$$D = f(M) + E, \quad (3)$$

where D is the observed data with observation error E, $f(\cdot)$ is the forward model operator, and M represents the model parameters, assuming that the observation error is a random variable with a mean of 0, and the systemic error induced by the iteration of the forward operator is much smaller than the detector error. For systems with unknown errors, assuming a Gaussian distribution is a reasonable choice. It is assumed that the observation error satisfies $E \sim N(0, \Gamma)$, where Γ is the covariance matrix and n is the number of detectors. Therefore, the likelihood function can be expressed as follows:

$$p(D|M,I) = \frac{1}{(2\pi)^{n/2} \det(\Gamma)^{1/2}} \exp\left\{-\frac{[D-f(M)]^{\mathrm{T}}[D-f(M)]}{2\Gamma}\right\}. \quad (4)$$

2.3. Markov Chain Monte Carlo Sampling. After parameter identification using Bayesian inference, the posterior probability distribution (PPD) provides information related to pollution sources, such as their position and intensity. When the PDF has a simple form, an analytical solution can be obtained directly. However, for high-dimensional nonlinear systems, the PDF is often relatively complex and difficult to solve, making it challenging to obtain effective information [29]. Parameter estimation methods can be used to obtain the solution; typically, there are maximum likelihood estimation and sampling statistics methods [30]. For maximum likelihood estimation, the PDF $p(D|M,I)$ is maximized by finding a suitable M. For sampling statistics methods, a group of samples satisfying the posterior PDF is extracted. The statistical characteristics of the posterior PDF can be obtained by analyzing the samples, and the estimated values of pollutant source information can be obtained accordingly. Therefore, efficient and accurate sampling from the posterior PDF is critical for parameter inversion using Bayesian inference.

Common sampling statistical methods include Markov chain Monte Carlo sampling (MCMC), acceptance-rejection sampling, and importance sampling [28]. In this paper, the MCMC method is utilized as an effective approach for Bayesian inference to estimate the posterior distribution $p(D|M,I)$ of interest parameters through random sampling in probability space. Samples that follow the target distribution $p(D|M,I)$ can be obtained by constructing one or more Markov chains, and then the numerical solution of the posterior PDF is obtained through statistical analysis of the samples. When applying this method to the inverse problem of indoor environment, the Metropolis-Hastings MCMC is an effective and widely-used algorithm, with its pseudocode shown in Algorithm 1. The flow chart in Figure 1 illustrates the methodology for identifying the location and release intensity of a pollutant source through Bayesian influence.

2.4. Source-Detector Relationship. When using Bayesian inference to estimate pollution source, it is necessary to perform multiple calculations of the forward pollutant advection-diffusion equation (Equation (5)) to obtain the numerical solutions of the pollutant distribution with different source parameter conditions (such as source location, intensify, and release time). Without the aid of a surrogate model, performing only CFD calculations (Equation (5))

1: initial parameters: $m^{(0)}$
2: FOR k = 0,1,2, … DO {Sampling from Proposed Distribution}
3: $m^* \longleftarrow$ sampling from $q(\cdot|m^{(k)})$
4: $\alpha \longleftarrow \min\left[1, (p(m^*|d,I)/p(m^{(k)}|d,I))(q(m^{(k)}|m^*)/q(m^*|m^{(k)}))\right]$ {Calculate acceptance rate}
5: $u \longleftarrow$ *sampling from* uniform(0, 1)
6: IF $u < a$ THEN
7: $m^{(k+1)} \longleftarrow m^*$ {Accept Sampling}
8: ELSE
9: $m^{(k+1)} \longleftarrow m^{(k)}$ {Reject Sampling}
10: END IF
11: END FOR

Algorithm 1: Metropolis-Hastings MCMC.

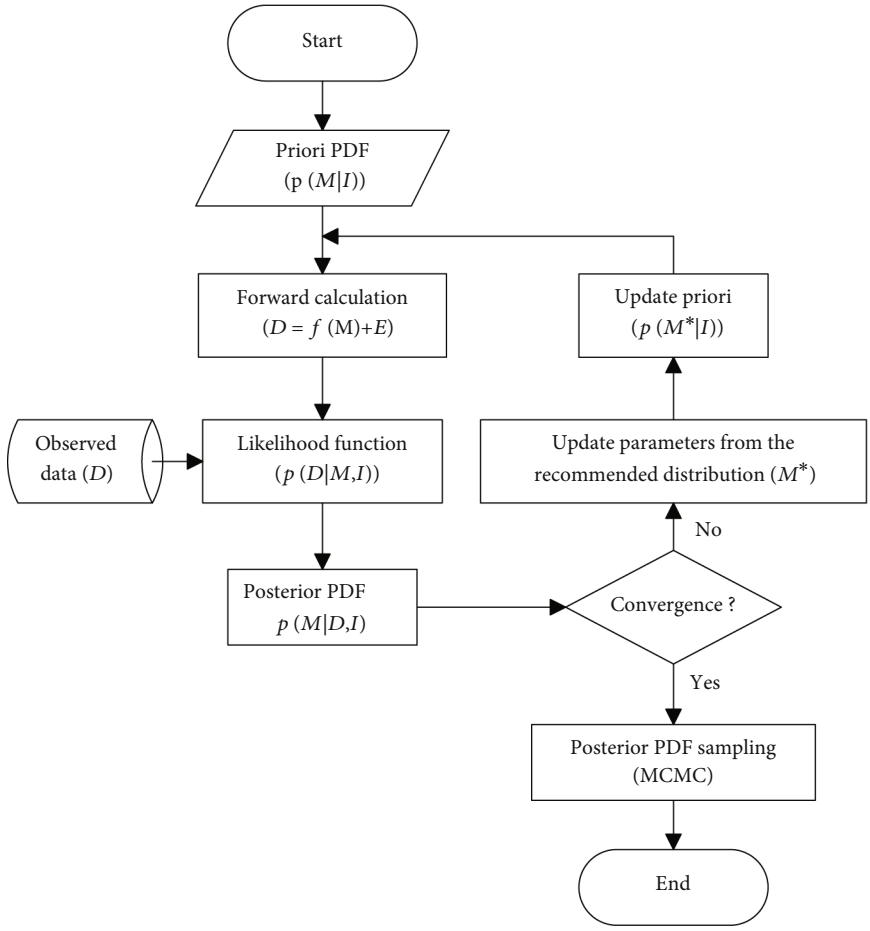

Figure 1: Solution flowchart to inversely identify the pollutant source information in the bionic ventilation system using Bayesian inference.

can be computationally expensive, often requiring tens of thousands or even hundreds of thousands of forward calculations. When faced with high-dimensional problems and complex domains, implementing this method can become challenging, which contradicts the need for timely and accurate source location. In addition, the forward calculation can obtain information about the entire flow field, while the monitoring points in the flow field are often sparse, resulting in only a few monitoring points' information being used for source term estimation. In this paper, dual adjoint models of transient pollutant transport in dynamic fields are constructed to increase the amount of information obtained in a single calculation process.

$$\begin{cases} \dfrac{\partial C}{\partial t} + \vec{u} \cdot \nabla C = \nabla \cdot (D \nabla C) + S, & \forall \left(\vec{x}, t\right) \in \Omega \times [0, T], \\ \nabla C \cdot \vec{n} = 0, & \forall \left(\vec{x}, t\right) \in \Gamma \times [0, T], \\ C\left(\vec{x}, 0\right) = C_0, & \forall \left(\vec{x}, t\right) \in \Omega \times [0, t_s), \end{cases} \tag{5}$$

where the source term in Equation (5) is assumed to be an instantaneous source and can be expressed as follows:

$$S = q_s \delta\left(\vec{x} - \vec{x}_w\right)[H(t - t_s) - H(t - t_e)], \tag{6}$$

where q_s is the source intensity, kg/s, t_s is the start release time, and t_e is the end release time $(t_s, t_e \in [0, T])$. $\vec{x}_w$ is the source location, $\vec{x}_w \in \Omega$. $\delta(\cdot)$ and $H(\cdot)$ are the Dirac delta and Heaviside unit step functions, respectively.

$$\delta\left(\vec{x} - \vec{x}_w\right) = \begin{cases} 1, \vec{x} = \vec{x}_w, \\ 0, \vec{x} \neq \vec{x}_w, \end{cases} \qquad H(\tau) = \begin{cases} 1, \tau \leq 0, \\ 0, \tau > 0. \end{cases} \tag{7}$$

The advection-diffusion equation (Equation (5)) models the release of the source S over a space-time domain $\Omega \times [0, T]$ through the time evolution of the concentration field, C. Here, C denotes a Reynolds-average concentration, kg/m^3, and $\vec{u}$ denotes the Reynolds-average wind velocities, m/s. t denotes time, s, and C_0 is the initial pollutant concentration, kg/m^3. D is an eddy diffusivity used to model the turbulent scalar fluxes, kg/(m^3 s). Ω is the fluid domain, and Γ is the boundary of the spatial domain. The vector $\vec{n}$ refers to the boundary-normal direction, and $\nabla(\cdot)$ is a gradient operator.

The forward advection-diffusion operator L is defined as Equation (8) which describes the linear, one-to-one, nonsingular, nonreactive pollutant transport equation.

$$L(\cdot) = \frac{\partial}{\partial t}(\cdot) + \vec{u} \cdot \nabla(\cdot) - \nabla \cdot (D\nabla(\cdot)) \Longrightarrow L(C) = S. \tag{8}$$

When the source release position is fixed, the concentration distribution C and the concentration values of the detectors form a linear system, which naturally satisfies the superposition and homogeneity of a linear system. Assuming that the value of the ith detector at $\vec{x}_r$ is DS_i, it can be expressed as the inner product of the concentration field C and the detector response function R, as follows:

$$\mathrm{DS}_i = \langle C, R \rangle = \int_0^T \mathrm{d}t \int_\Omega \mathrm{CR} d\Omega. \tag{9}$$

The response function of any detector is expressed as R, with units of 1/(m^3 s), as Equation (10), which acts as a space-time filter and would be a Dirac delta function in both space and time for an ideal detector with infinite space and temporal resolving power. In other words, it is assumed that at t_r and $\vec{x}_r$, the nominal pollution source (detector) has unit intensity.

$$R = R\left(\vec{x} - \vec{x}_r, t - t_r\right) = \delta\left(\vec{x} - \vec{x}_r\right) \cdot \delta(t - t_r). \tag{10}$$

By multiplying the dual adjoint concentration C^* of forward transport (Equation (5)) and integrating over the space-time domain, the dual adjoint equation was obtained as Equation (11). From a physical point of view, the dual adjoint equation is the inverse of the forward advection-diffusion equation (Equation (5)) with respect to time and convection terms. The general procedure for obtaining the dual adjoint of a linear operator is outlined in [31].

$$\begin{cases} -\dfrac{\partial C^*}{\partial t} - \vec{u} \cdot \nabla C^* = \nabla \cdot (D\nabla C^*) + R, & \vec{x} \in \Omega \times [0, T], \\ D\nabla C^* \cdot \vec{n} + \vec{u} \cdot \vec{n} C^* = 0, & \vec{x} \in \Gamma \times [0, T]. \end{cases} \tag{11}$$

The dual adjoint operator L^* is defined as follows:

$$L^*(\cdot) = -\frac{\partial}{\partial t}(\cdot) - \vec{u} \cdot \nabla(\cdot) - \nabla \cdot (D\nabla(\cdot)) \Longrightarrow L(C^*) = R. \tag{12}$$

According to the Lagrangian dual relation [32], DS_i could also be expressed as the inner product of the dual adjoint concentration field C^* and the source strength S, expressed as follows:

$$\mathrm{DS}_i = \langle S, C^* \rangle = \int_0^T \mathrm{d}t \int_\Omega \mathrm{SC}^* d\Omega. \tag{13}$$

Then,

$$\langle C, L^* C^* \rangle = \langle \mathrm{LC}, C^* \rangle \Longrightarrow \langle C, R \rangle = \langle S, C^* \rangle. \tag{14}$$

When the pollutant transport system is unsteady, the forward pollutant advection-diffusion operator $L(\cdot)$ equals to $\partial(\cdot)/\partial t + \vec{u} \cdot \nabla(\cdot) - \nabla \cdot (D\nabla(\cdot))$, and the dual adjoint operator $L^*(\cdot)$ equals to $-\partial(\cdot)/\partial t - \vec{u} \cdot \nabla(\cdot) - \nabla \cdot (D\nabla(\cdot))$. Then, the value of the ith detector at $\vec{x}_r$ position t_r moment is $DS_i^{(t_r)}$.

Under the assumption that the timescale of pollutant concentration transport is significantly shorter than that of the flow field, it is inferred that the pollution source disperses within a relatively stable quasisteady-state velocity field. According to the principle of superposition,

$$F_i^{(t_r)} = \sum_{t=t_s}^{t_r} C\left(\vec{x}_r, t_r, \vec{x}_w, t_s\right) Q(t_s), \tag{15}$$

where $C(\vec{x}_r, t_r, \vec{x}_w, t_s)$ is the concentration value measured at monitoring point $\vec{x}_r$ at time t_r after unit source intensity released at $\vec{x}_w$ and time t_s. $F_i^{(t_r)}$ is the detector value measured at the ith monitoring point at time t_r when the source intensity is $Q(t_s)$. It can be seen that $F_i^{(t_r)}$ is the integral of the product of the unit source intensity field and the source intensity over the time period $[t_s, t_r]$.

In practice, the detector does not obtain the concentration values continuously but rather measures the average value

over a period of time. Similar to the superposition in Equation (15), the detector value $DS_i^{(t_r)}$ measured at the ith monitoring point at $\vec{x}_r$, at time t_r, can be expressed as follows:

$$\begin{aligned} \mathrm{DS}_i^{(t_r)} &= \int_{t_s}^{t_r} q_s(t) C^*\left(\vec{x}_r, t_r, \vec{x}_w, t\right) \mathrm{d}t \\ &= \sum_{t=t_s}^{t_r} C^*\left(\vec{x}_r, t_r, \vec{x}_w, t\right) q_s(t) \Delta t, \end{aligned} \tag{16}$$

where $C^*(\vec{x}_r, t_r, \vec{x}_w, t)$ is the concentration value of monitoring point $\vec{x}_w$ at time t, after the unit intensity source is released from location $\vec{x}_r$ at time t_r.

When n cases with different release times $(t_{s1}, t_{s1}, \cdots, t_{sn})$ and different release positions $(\vec{x}_{w1}, \vec{x}_{w2}, \vec{x}_{w3}, \cdots, \vec{x}_{wn})$ are needed to be calculated, Bayesian inference determines the next state parameter m^* according to the current state parameter $m^{(k)}$ with the help of proposal distribution. n^2 forward calculations are needed to complete all possible cases. In contrast, Bayesian inference with source-receptor relationships assumes a nominal pollution source with unit intensity at the monitoring positions. It is only necessary to calculate the dual adjoint concentration field of the nominal source $C^*(\vec{x}_r, t_r, \vec{x}_w, t)$ once, and then, according to the dual relation of Equation (16), the concentration at any source intensity, position, and release time can be obtained for the monitors $\vec{x}_r$.

Therefore, the significance of introducing the unsteady dual adjoint equation is that the problem of solving for multiple source parameters (position $\vec{x}_w$, intensity q_s, and release time t_s) in the forward advection-diffusion equations is transformed into the problem of solving for multiple physical field parameters (monitoring point $\vec{x}_r$ and transport time Δt) of dual adjoint equations, which greatly reduces the consumption of computing resources.

When the intensity of the pollutant source is constant and released at time $t_s = 0$, the S is equal to $q_s\delta(\vec{x} - \vec{x}_w)$; then,

$$\mathrm{DS}_i^{(t_r)} = q_s \sum_{t=0}^{t_r} C^*\left(\vec{x}_r, t_r, \vec{x}_w, t\right) \Delta t. \tag{17}$$

The difference and connection between the dual adjoint equation and the forward transport equation can be physically explained as follows: the forward transport equation describes the pollutant concentration distribution caused by an exact pollution source to any position in the domain, while the dual adjoint equation describes the influence of any potential source on the pollutant concentration in the domain. The forward equation and the adjoint equation reflect the same phenomenon from different angles. If the forward transport results of a given source are needed to be evaluated, it is convenient to use the forward transport equation to evaluate. If the source position is uncertain, then the dual adjoint equation has a unique advantage.

3. Computational Fluid Dynamics and Its Solver Settings

3.1. Computational Geometry. The characteristics of a bionic ventilation system, inspired by the respiratory system of humans and animals, were assessed in a rectangular enclosure based on the IEA Annex 20 experiment, as shown in Figure 2 [33]. This system utilizes time-periodic supply velocity in a mixing ventilation flow, and the feasibility of applying Bayesian inference for pollutant source identification in such systems was verified. The experimental setup consisted of a 9.0 m × 3.0 m × 3.0 m ($L \times H \times W$) rectangular enclosure with air supplied through a 0.168 m high linear opening and exhausted through a 0.48 m height linear exhaust located opposite the supply opening, as illustrated in Figure 3. This model represents a typical forced convection mixing ventilation system with adiabatic boundaries.

Drawing inspiration from the periodic inhalation and exhalation of air through a single "pipeline system" in humans and animals, the characteristics of periodic ventilation were extended to indoor ventilation systems, resulting in bionic ventilation systems. Two typical types of bionic systems were proposed, based on traditional mixing ventilation, as shown in Figure 4, including single-side ventilation system and dual-side ventilation system. To estimate unknown pollutant sources in unsteady airflow fields, this paper presents a Bayesian inference method suitable for a bionic ventilation system. It is assumed that two constant pollutant sources are released in this bionic ventilation system: source-1 at (2.3 m, 2.6 m) and source-2 (6.5 m, 1.2 m). Three sensors are installed within the room: sensor-1 at the ceiling (5.8 m, 2.8 m), sensor-2 at the floor (2.3 m, 0.2 m), and sensor-3 at the exhaust vent (8.8 m, 0.24 m), as depicted in Figure 4. Sensors play a critical role in the inverse identification of indoor pollutants. The primary aim of this study is to present a novel Bayesian inference inverse method that is suitable for the strong nonlinearity inherent in bionic ventilation systems. In this paper, we have employed sensors with unlimited resolution. The effects of their quantity, placement, and accuracy on the results of pollutant inverse identification will be the subject of future research.

3.2. Boundary Conditions. In this paper, two types of time-periodic supply velocity were utilized, based on a sine function and a rectangular wave function, as illustrated in Figure 5. The sine function generated a time-periodic supply velocity that oscillates with a period P and amplitude A around a constant reference velocity $U_0 = 0.455$ m/s, defined by Equation (18). The rectangular wave function, a superposition form of the sine function, is convenient to implement in practice with 0-1 controller. The period P and amplitude A also serve as key parameters determining the air supply law, and the function is described by Equation (19). In the case of dual-side ventilation, the left and right vents operate with a half-period phase difference. Specifically, when the left vent reaches its maximum velocity, the right vent is at their minimum velocity.

Figure 2: The experimental schematic diagram of IEA Annex 20.

$$u = A \times U_0 \sin\left(\frac{2\pi t}{P}\right) + U_0, \tag{18}$$

$$u = \begin{cases} 0.455 \times A & n\mathrm{T} < t \le n\mathrm{T} + \left(\frac{\mathrm{T}}{2}\right), \\ 0 & n\mathrm{T} + \left(\frac{\mathrm{T}}{2}\right) < t \le n\mathrm{T} + \mathrm{T}. \end{cases} \quad n = 0, 1, 2, \cdots. \tag{19}$$

The influence of varying periods P for both sine and rectangular wave functions were investigated in this paper, ranging from $0.003\tau_n$ to $0.3\tau_n$, where τ_n denotes the nominal time constant [34], which represents the shortest time required to replace the air in an enclosure, as defined by Equation (20). V is the volume of the enclosure, and Q is the volume rate supplied. The case setup for three different ventilation systems is depicted in Table 1.

$$\tau_n = \frac{V}{Q}. \tag{20}$$

The supply condition for turbulent kinetic energy k was determined by Equation (21). $\bar{u}_{\mathrm{ref}}$ is the average reference velocity, m/s. In this paper, the turbulence intensity (I) was set at 10%, which typically falls within the range of 1-10%. The turbulent dissipation rate ε at the supply was calculated using Equation (22) [35]. The supply temperature was set to 20°C with the kinematic viscosity ν being 15.3×10^6 m^2/s. L is 3 m as the characteristic length, C_μ 0.09 in this paper.

$$k = \frac{3}{2}(\bar{u}_{\mathrm{ref}} I)^2, \tag{21}$$

$$\varepsilon = C_\mu^{3/4} \frac{k^{3/2}}{0.01\mathrm{L}}. \tag{22}$$

Using the source-detector relationship (described in Section 2.4) can improve MCMC sampling efficiency for Bayesian inference. It is critical to solve the dual adjoint equation accurately, but its accuracy is significantly influenced by the boundary conditions, particularly near the domain boundary. As shown in Equation (11), $D\nabla C^* \cdot \vec{n} + \vec{u} \cdot \vec{n} C^* = 0$ serves as a mixed boundary condition and is solved using Fluent software with appropriate numerical settings [36]. In Fluent, the grid element c_0 attached to the boundary is depicted in Figure 6, where $\vec{e}_s$ is a vector connecting the centroid of cell c_0 to the face centroid, $\vec{n}$ is the unit normal vector in the direction from c_0 to the boundary face f, and d_r is the distance that connecting the centroid of cell c_1 to the face centroid.

Under mixed boundary conditions, for a generic cell c_0 adjacent to the boundary, the diffusive flux across the boundary face f of the cell is expressed as follows:

$$\int_f D\left(\frac{\partial C^*}{\partial n}\right) dS + \int_f u_n C^* dS = 0. \tag{23}$$

Using the midpoint rule of surface integral, the diffusive flux can be approximated as Equation (24), where D_f is the diffusion coefficient at the boundary, A_f is the area of the boundary grid, and u_n is the velocity component perpendicular to the boundary.

$$D_f\left(\frac{\partial C^*}{\partial n}\right)_f A_f + u_n C^* A_f = 0. \tag{24}$$

The diffusive flux is approximated in two parts: the primary gradient term and the secondary gradient (cross-diffusion) term. The primary gradient is evaluated implicitly along the line connecting the cell centroid c_0 to the centroid face f. It is corrected by a secondary gradient term, which is evaluated explicitly using the gradient obtained from the previous iteration, as shown in the following equation.

$$D_f\left(\frac{\partial C^*}{\partial n}\right)_f A_f \approx \underbrace{D_f \frac{\left(C_f^* - C_{c0}^*\right)}{\mathrm{dr}} \left(\frac{\vec{A} \cdot \vec{A}}{\vec{A} \cdot \vec{e}_s}\right)}_{\text{primary}} + \underbrace{D_f \left(\overline{\nabla C^*} \cdot \vec{A} - \overline{\nabla C^*} \cdot \vec{e}_s \frac{\vec{A} \cdot \vec{A}}{\vec{A} \cdot \vec{e}_s}\right)}_{\text{secondary}}. \tag{25}$$

By substituting Equation (25) into Equation (24), boundary conditions for dual adjoint equations can be expressed as shown in Equation (26), where β_0 is the secondary term and A_{be} equals to $\vec{A} \cdot \vec{A} / \vec{A} \cdot \vec{e}_s$

$$C_f^* = \frac{D_f (A_{\mathrm{be}}/\mathrm{dr}) C_{c_0}^* - \beta_0}{u_n A_f + D_f (A_{\mathrm{be}}/\mathrm{dr})}. \tag{26}$$

3.3. Computational Settings and Parameters. The experiment depicted in Figure 2 was modeled in 2D based on the information provided by reference [37]. The problem was simulated by ANSYS Fluent 2022R2 and treated as a transient model with a time step size of 0.01 seconds. The number of iterations within each time step was set to 20. The adequacy of both the iteration count and the sampling time (100 periods) was confirmed by monitoring the development of instantaneous and time-averaged velocities. The RNG $k-\varepsilon$ turbulent model was employed for the URANS

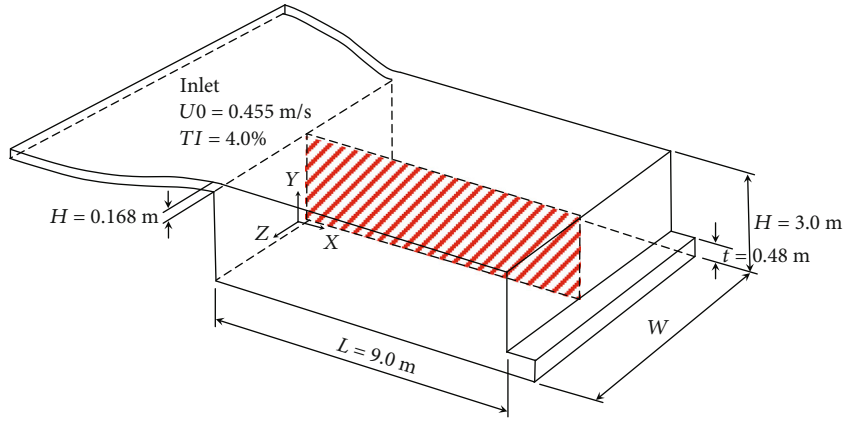

Figure 3: Vertical cross-section of IEA Annex 20 geometry established in CFD.

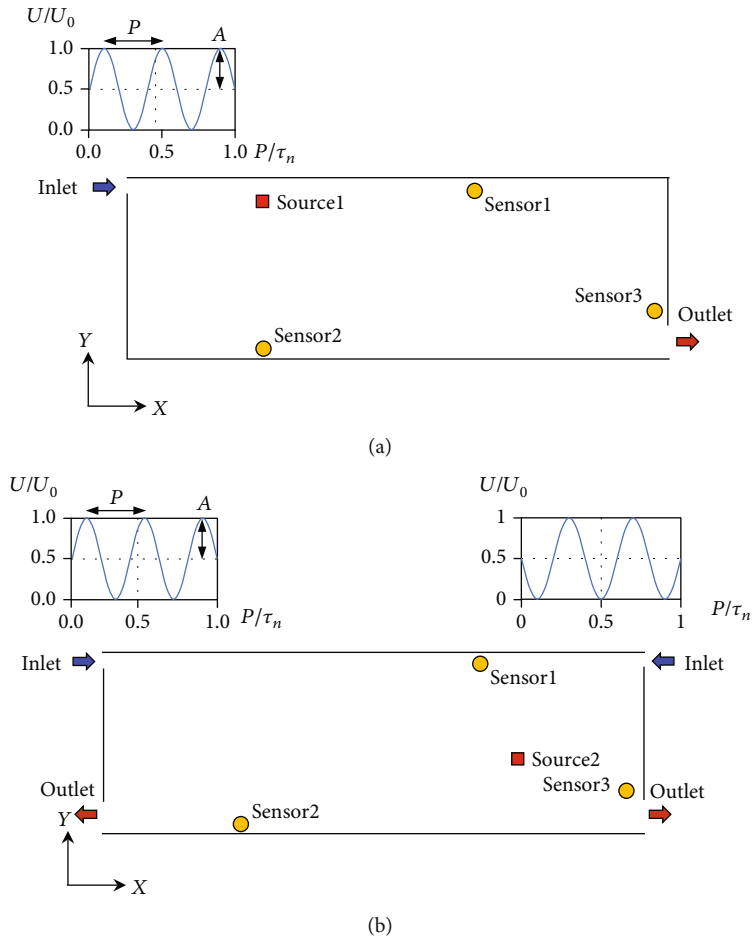

Figure 4: Two proposed bionic ventilation systems: (a) single-side ventilation system and (b) dual-side ventilation system.

simulations, in which discretization schemes and pressure interpolation are second order, and the SIMPLE algorithm was used for pressure-velocity coupling. In Fluent, we employed the user-defined function (UDF) approach to solve both the pollutant transport equation and the corresponding dual adjoint equation. The pollutant source was addressed using the user-defined scalar source term. All boundary conditions for the pollutant transport equation were set to the Neumann boundary conditions, ensuring the diffusive flux across the boundary face was zero. Commonly used RNG $k-\varepsilon$ models determine the turbulent kinetic energy k and the turbulent dissipation rate ε by solving Equations (27) and (28), subsequently obtaining the turbulent viscosity using Equations (29).

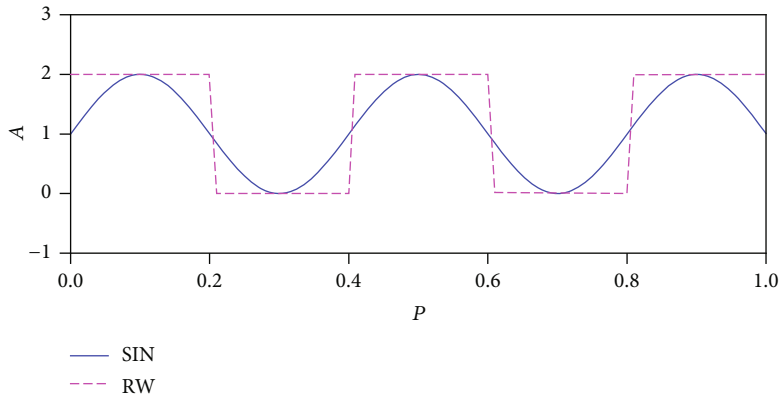

Figure 5: Time-periodic supply velocity profiles for the sine function (SIN) and the rectangular wave function (RW).

Table 1: Case setup for three different ventilation systems.

Type	Flow rate (m^3/s)	ACH (1/h)	Time-periodic (s)	Source information (x, y)[a]	S[b]
Constant	0.0764	0.0028	—	—	—
Single-side	0.0764	0.0028	$0.003\tau_n$~$0.3\tau_n$	(2.3, 2.6)	10.0
Dual-side	0.0764	0.0028	$0.003\tau_n$~$0.3\tau_n$	(6.5, 1.2)	5.0

[a]Unit of the source location is m. [b]Unit of the source location is mL/s.

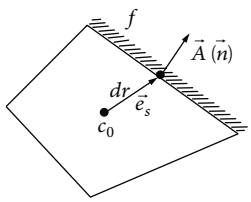

Figure 6: Numerical description of mixed boundary conditions for dual adjoint equations.

$$\frac{\partial}{\partial t}(\rho k) + \frac{\partial}{\partial x_i}(\rho k u_i) = \frac{\partial}{\partial x_j}\left[\left(\mu + \frac{\mu_t}{\sigma_k}\right)\frac{\partial k}{\partial x_j}\right] + G_k + G_b - \rho\varepsilon - Y_M + S_k, \tag{27}$$

$$\frac{\partial}{\partial t}(\rho \varepsilon) + \frac{\partial}{\partial x_i}(\rho \varepsilon u_i) = \frac{\partial}{\partial x_j}\left[\left(\mu + \frac{\mu_t}{\sigma_\varepsilon}\right)\frac{\partial \varepsilon}{\partial x_j}\right] + C_{1\varepsilon}\frac{\varepsilon}{k}(G_k + C_{3\varepsilon}G_b) - C_{2\varepsilon}\rho\frac{\varepsilon^2}{k} + S_\varepsilon, \tag{28}$$

$$\mu_t = \rho C_\mu \frac{k^2}{\varepsilon}, \tag{29}$$

where $i, j = 1, 2, 3$. C_μ is a constant. ρ is the density. u is velocity. G_k represents the turbulent kinetic energy generated by the mean velocity gradient, while G_b denotes the turbulent kinetic energy produced by buoyant forces. Y_M is the dissipation rate due to fluctuating expansion in compressible flows, but this is typically neglected in indoor environment. The model constants are given as $C_{1\varepsilon} = 1.44$, $C_{2\varepsilon} = 1.92$, and $C_\mu = 0.09$. The turbulent Prandtl numbers for k and ε are $\sigma_k = 1.0$ and $\sigma_\varepsilon = 1.3$, respectively. These default values, informed by turbulence experiments, are notably effective for wall shear flow problems. S_k and S_ε act as user-defined source terms.

4. Verification and Validation with Benchmark Experiments

Since the simplified geometry of the IEA Annex 20 experiment, the mesh was composed of quads elements in a uniform distribution (structure mesh) and was refined near the walls to accurately transfer the boundary conditions to the air domain. Velocity gradients are particularly large in the regions adjacent to the walls; therefore, a finer mesh is necessary for accurate predictions. The fluid domain was discretized using grids, with the first layer situated 0.01 m from the wall and a grid growth rate of 1.05. Wall functions were employed to handle the transition of physical quantities from the wall to the turbulent core area, and the grids were refined near the wall to ensure $Y+$ values were greater than or equal to 11.63. In this paper, scalable wall functions are adopted, which can effectively prevent numerical deterioration near the wall [36].

Figure 7 presents the velocity field for the initial experiment case with a constant inlet velocity of 0.455 m/s. A clockwise airflow with a strong jet throw beneath the ceiling is observed, resulting from the air inlet. Grid independency verification was performed for mesh sizes of 90×30 ($L \times H$), 150×50 ($L \times H$), and 240×80 ($L \times H$). Figure 8 depicts the

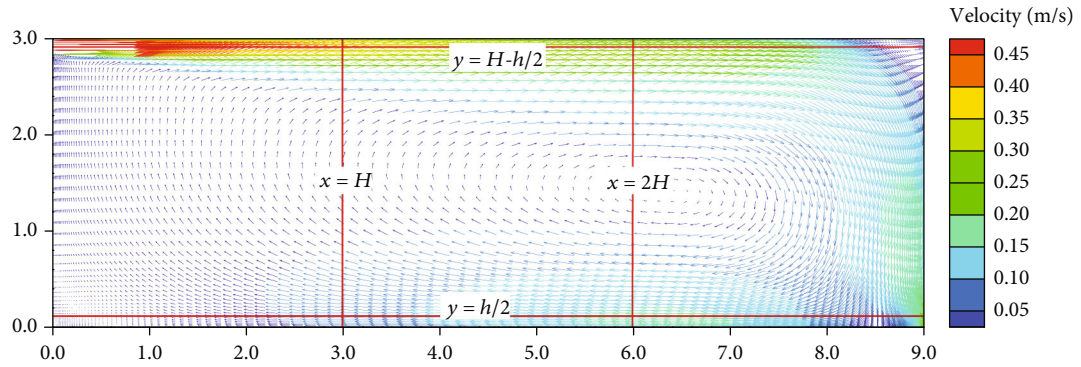

Figure 7: Velocity vector distribution at the vertical cross-section velocity vector distribution at the vertical cross-section range from 0.05 m/s to 0.45 m/s.

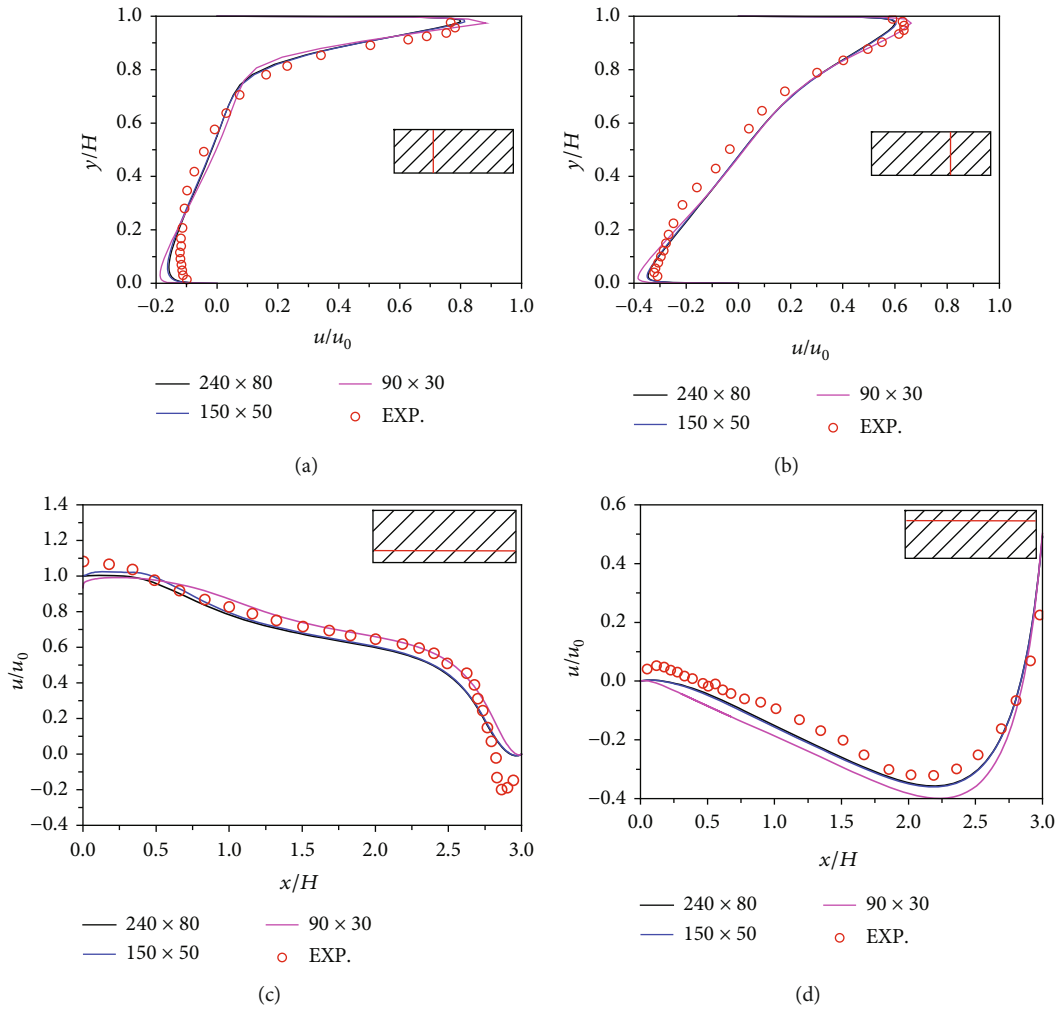

Figure 8: Numerical verification results at four reference lines and a grid independence test with three different grid numbers.

dimensional velocity u/u_0 obtained from the 2D steady RANS CFD simulations at four different reference positions (red lines): $x = H$, $x = 2H$, $y = h/2$, and $y =$ H-h/2. Relevant experimental data can be obtained from https://www.cfd-benchmarks.com. Detailed discussions on data processing and comparisons can also be found in References [37–42]. Various turbulence models have been adopted for comparison, including the standard $k-\varepsilon$ model, low-Reynolds $k-\varepsilon$ model, RNG $k-\varepsilon$ model, standard $k-\omega$ model, and SST $k-\omega$ model. In addition, LES, RANS, and URANS were also compared. Generally, the $k-\varepsilon$ models outperformed the $k-\omega$ models. URANS $k-\varepsilon$ and LES demonstrated higher

predictive accuracy compared to RANS $k-\varepsilon$. In this research, good agreement is present along the four reference lines for u/u_0, with the largest discrepancies near the floor and ceiling of the enclosure and the best agreement in the wall jet region. The average difference between simulated and experimental data is 5.2% for 150×50 mesh, which is negligible. However, the CFD model with a 90×30 mesh predicted slightly worse results, particularly near the walls. After evaluating the overall performance, a mesh size of 240×80 was chosen for the CFD validation process. In Reference [37], several turbulence models, standard $k-\varepsilon$, RNG $k-\varepsilon$, realizable $k-\varepsilon$, standard $k-\omega$, and SST $k-\omega$, were adopted and compared for predicting flow patterns. Overall, the velocities predicted by all evaluated $k-\varepsilon$ and $k-\omega$ models are in good agreement with the measured velocities. However, significant differences in predicted velocities among the turbulence models are observed close to the top and bottom walls. In this region, the standard $k-\varepsilon$ and RNG models accurately predict the reverse flow near the floor and the jet throw near the ceiling, showing the best performance with differences of less than 7% compared to the experimental data. In contrast, the realizable $k-\varepsilon$ model exhibits the largest discrepancies, with differences of 21.3%. In this paper, the validation study demonstrates that the RNG $k-\varepsilon$ turbulent model, combined with the other computational settings and parameters employed, is sufficiently capable of predicting mixing ventilation flow in a genetic enclosure with adequate accuracy, particularly with respect to mean velocities. Therefore, the employed turbulent model and settings were used in the case study in the subsequent section.

5. Results and Discussion

5.1. Characteristic Analysis of Bionic Ventilation System from Direct CFD Models. This paper compares the typical characteristics of single-side and dual-side bionic ventilations, such as air age and inhomogeneity coefficient under different periodic conditions. The definitions of air age and supply air uniformity index were established. "Air age" was proposed by Sandberg in the 1980s and is defined as the time required for air to reach a specific location in a room from the supply vent [43]. This metric reflects the freshness of indoor air; the lower the air age at a particular location, the fresher the air in that location. Equation (30) presents the tensor expression of the air age equation [44].

$$\frac{\partial \tau}{\partial t} + \frac{\partial}{\partial x_i}(u_i \cdot \tau) = \frac{\partial}{\partial x_i}\left(\Gamma_A \cdot \frac{\partial \tau}{\partial x_i}\right) + 1, \tag{30}$$

where τ is air age at any point in the room (s); t is the time (s); u_i is the velocity component in the i direction (m/s); x_i is the spatial coordinate in the i direction ($i = 1, 2$); Γ_A is the diffusion coefficient of air age (m^2/s).

Air age demonstrates significant inhomogeneity within the fluid zone, and this inhomogeneity is reflected in the inhomogeneity coefficient, which can be expressed using Equation (31). In this equation, a_i represents the air age at a sampling point, $\bar{a}$ is the average value of air age, and N is the number of samples. The numerator of Equation (31) represents the RSME (root mean square error). Generally, a smaller inhomogeneity coefficient is desirable indoors.

$$k_a = \frac{\sqrt{\sum (a_i - \bar{a})^2 / N}}{\bar{a}}. \tag{31}$$

Figure 9 compares the time-averaged air age distribution of three different supply strategies after convergence and stabilization. Figure 9(a) displays the air age distribution with single-side constant supply ventilation. Influenced by the supply and exhaust vent layout, a unidirectional airflow vortex forms in the room. An air stagnation zone appears on the left side of the room, with a high air age of almost 500. Conversely, near the exhaust vent, air circulates well, resulting in a younger air age of almost 300. Traditional mixing ventilation, a common air supply method, is prone to short-circuiting of the airflow.

Regarding the bionic system with time-periodic supply velocity, Figures 9(b) and 9(c) display the air age distribution for single-side and dual-side supplies with a periodicity of $P = 0.03\tau_n$. Compared to constant supply, the bionic ventilation system with time-periodic supply resulted in a more uniform and younger air age distribution throughout most areas. The air age in most areas ranged between 200 and 400, demonstrating that the bionic ventilation system with time-periodic supply has significant advantages for improving indoor air quality compared to the traditional constant supply system.

Figure 10 displays the contours of the instantaneous air age for the case with a period of $P = 10\tau_n$, during one period after the time-average values have stabilized. Figure 10(a) shows periodic and fluctuating forward movement. Vortex rings carrying fresh air with high momentum move forward under the supply vent pushing, resulting in stronger mixing and purification abilities compared to traditional mixing ventilation. Figure 10(b) shows the contours of the dual-side bionic ventilation, which displays the back-and-forth movement of the flow in the enclosure, driven by the wall jets and the breakup of the recirculation vortex-rings. In comparison to single-side periodic ventilation, the stagnant regions of dual-side periodic ventilation appeared in the middle of each recirculation cell. Fresh air is delivered to the middle of the room due to the conflicting airflow from the dual-side vents and then spread along the floor until exhausted from the outlet.

Figure 11 presents a comparison of mean air age between single-side supply and dual-side supply with different sine time-periodic values from 0 to $0.3\tau_n$. For small time-periodic values ranging from 0 to $0.03\tau_n$, the mean air age decreases rapidly from 400 to 300. When the time periodicity exceeds $0.06\tau_n$, the air age no longer changes with the period and remains between 270 and 280. Dual-side ventilation exhibits a slight superiority over single-side, but both demonstrate nearly a 30% improvement compared to constant supply.

Figure 12 displays the inhomogeneity coefficient k_a with different time-periodic values for single-side supply and dual-side supply. Generally, the bionic ventilation system exhibits a smaller inhomogeneity coefficient than the

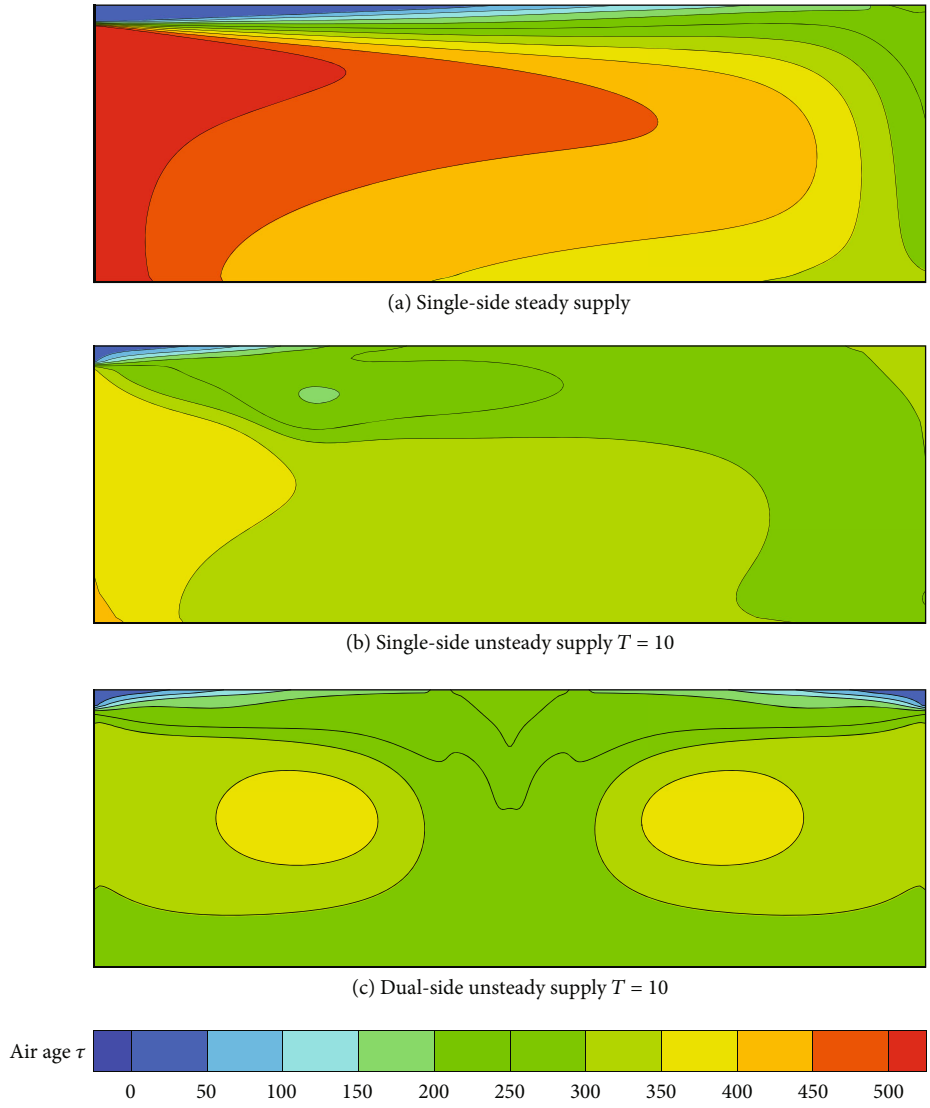

FIGURE 9: Air age comparison of different supply strategies. (a) Single-side ventilation with constant supply. (b) Single-side ventilation with time-periodic supply (sine function, $T = 0.03\tau_n$). (c) Dual-side ventilation with time-periodic supply (sine function, $T = 0 = 0.03\tau_n$).

constant supply. When the period is smaller than $0.06\tau_n$, k_a decreases with the increase in period. However, when the period exceeds $0.06\tau_n$, k_a slightly increases with the increase in period.

For the rectangular wave function time-periodic supply ventilation, Figures 13 and 14 demonstrate the air age and inhomogeneity coefficient. Compared to sine time-periodic supply, the rectangular wave function exhibits similar developmental phenomena, namely, a smaller air age and inhomogeneity coefficient compared to constant supply ventilation. As shown in Figure 15, rectangular wave function time-periodic single-side supply ventilation exhibits the smallest inhomogeneity coefficient compared to other cases, demonstrating a 77% decrease compared to constant supply. In dual-side ventilation for both sine and rectangular wave functions, the air age is larger than single-side, potentially due to a smaller air supply momentum compared to single-side in order to maintain the same air change rate (ACH). Overall, the bionic ventilation system demonstrates absolute advantages over the traditional constant supply system in air age and inhomogeneity coefficient.

5.2. Source Term Estimation Results from Inverse CFD Models. Traditional constant supply ventilation systems maintain a relatively stable indoor environment, making pollutant source estimation typically appropriate for steady indoor flow fields, although unsteady flow fields with minimal perturbations can also be assumed as steady flow fields [45]. However, bionic ventilation systems with time-periodic supply present a significant challenge for estimating pollutant sources in dynamic flow fields. In this paper, we proposed a novel Bayesian inference method suitable for bionic ventilation systems, which exhibit strong pulsation and unsteady characteristics. Single-side and dual-side time-periodic ventilations with a period of $P = 0 = 0.015\tau_n$ using a sine supply function were chosen as the typical

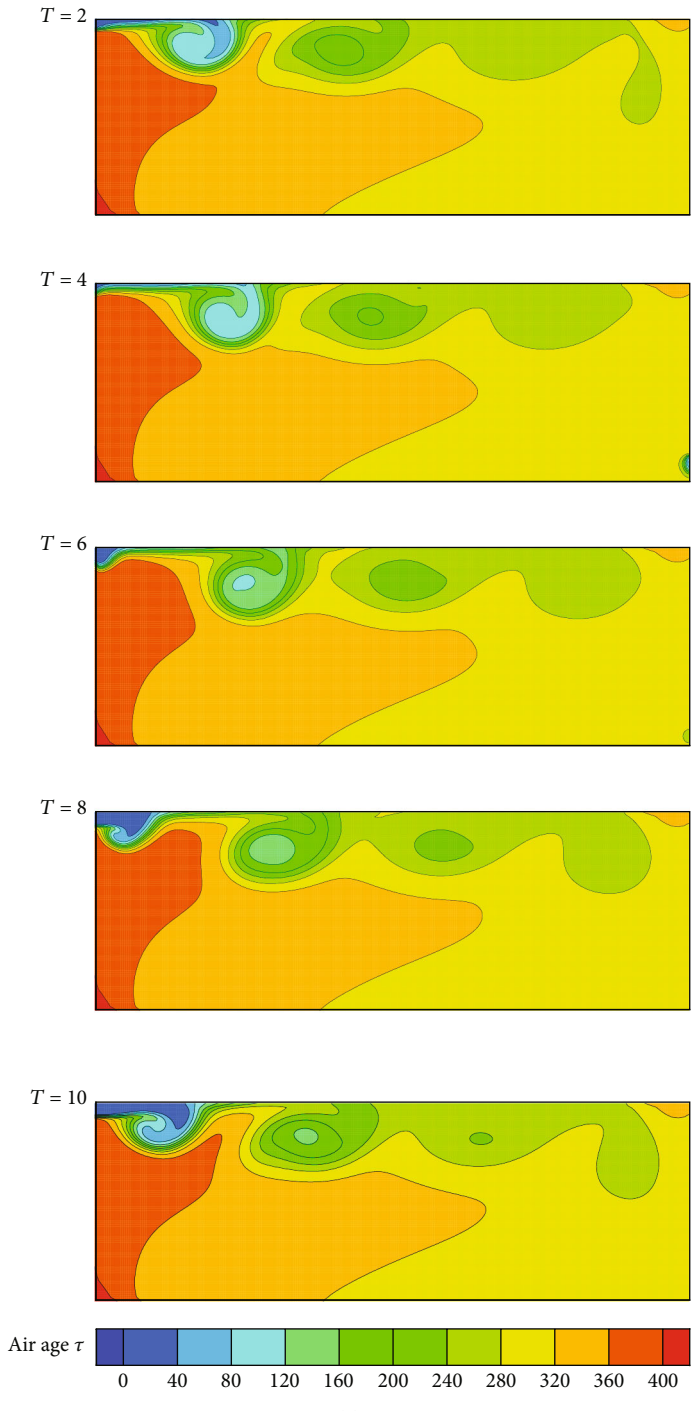

(a)

Figure 10: Continued.

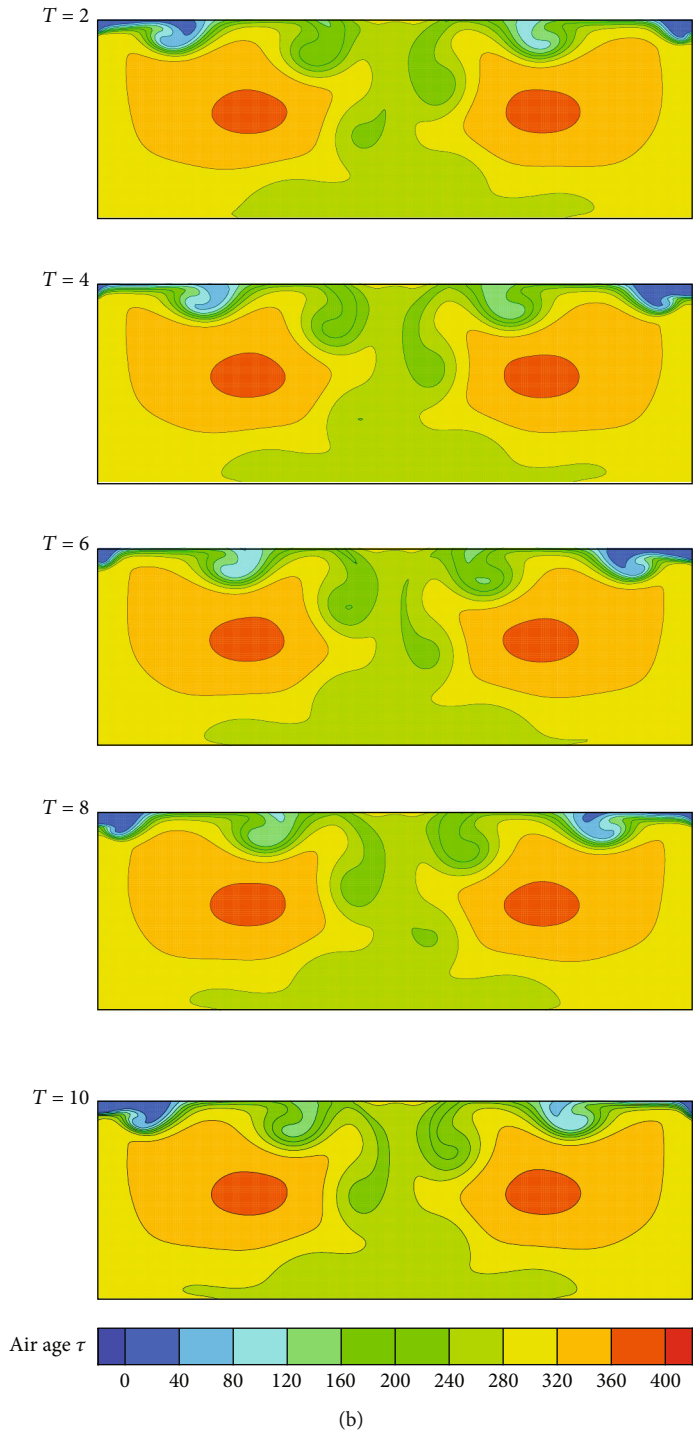

FIGURE 10: Contours of the instantaneous air age during one period T ($T = 0.03\tau_n$) for sine function. (a) Single-side periodic ventilation. (b) Dual-side periodic ventilation.

situations for source term estimation, given their high instability and nonlinearity characteristics.

Figure 16(a) shows the spatial variation of concentration at two vertical lines ($x = H$ m, $x = 2H$ m), resulting from a unit point source release at the sensor's location, which was solved using the dual adjoint Equation (11). To facilitate comparison, Figure 16(a) also shows the concentration predicted by solving the forward advection-diffusion Equation (5). From the figure, it is evident that the concentrations predicted by the dual adjoint Equation (11) agree well with those predicted by the forward Equation (5). Figure 16(b) illustrates the temporal variation of the concentration at three sensors after the source was released at time $t = 0$. It is apparent that the peak values of pollutants at each monitoring point occur at different times due to the indoor flow field. The time series of concentrations predicted by the dual

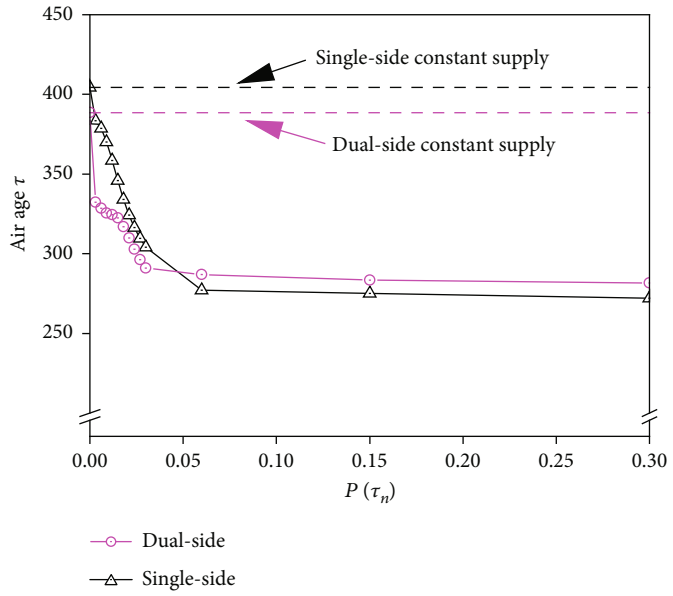

Figure 11: Mean air age with different time periods for single-side supply and dual-side supply bionic ventilation systems (sine function).

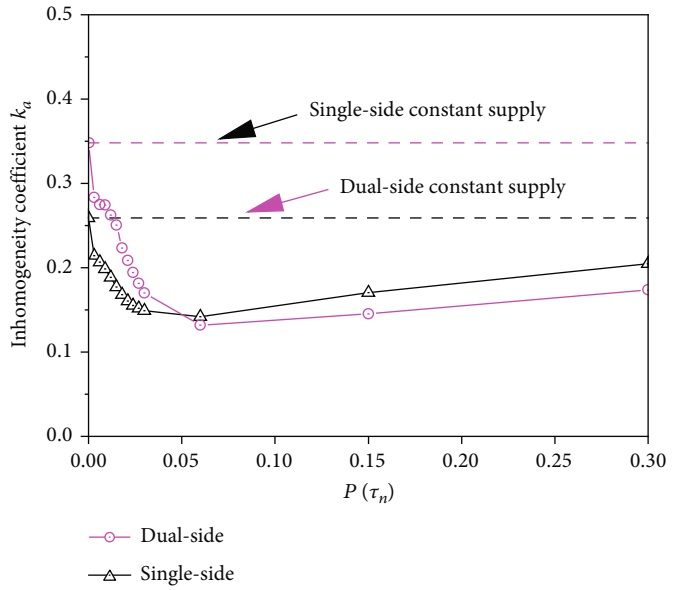

Figure 12: Inhomogeneity coefficient k_a with different time periods for single-side supply and dual-side supply bionic ventilation systems (sine function).

adjoint (Equation (5)) also exhibits a strong agreement with the forward time series.

Bayesian inference was employed to estimate source information, including source position and intensity, under dynamic flow fields. It is worth noting that the intensity of pollution sources exhibits a linearly relationship with the concentration at the monitoring point and can be calculated through linear scaling. Nevertheless, the intensity of pollution sources is still considered as a variable that needs to be identified through Bayesian inference.

The posterior probability density function (PDF) of the source position was obtained using the grid computing method [46] as shown in Figure 17. The posterior probability distribution (PPD) of the pollutant source exhibited a more extensive spread along the return airflow path. And the maximum posterior PDF was located near the actual source location: 2.3 m and 2.6 m for Figure 17(a) and 6.5 m and 1.2 m for Figure 17(b). The PPD effectively displays the results of identifying unknown parameters.

When the posterior PDF becomes more complex due to an increase in unknown parameters or system nonlinearity, analytical solutions become difficult to obtain and visualize. Conventional optimization methods often prove inefficient and limited in solving parameter identification problems with inaccurate prior information, large measurement, and numerical errors. Therefore, a sampling statistics method is

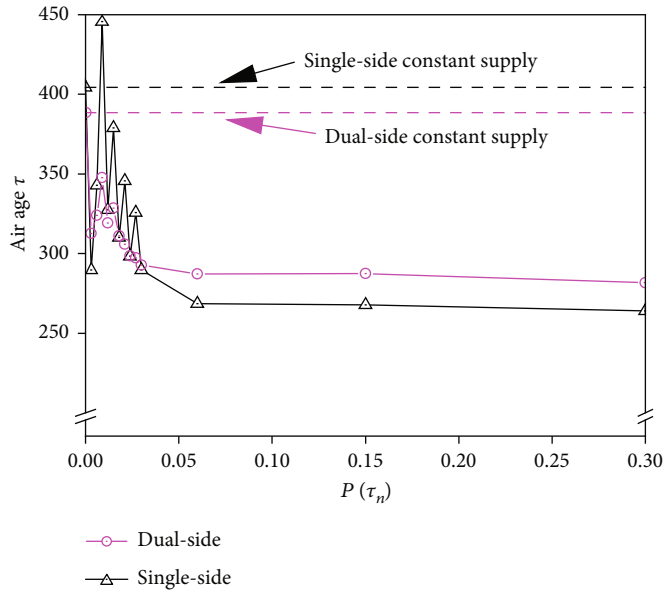

Figure 13: Mean air age with different time periods for single-side supply and dual-side supply bionic ventilation systems (square wave function).

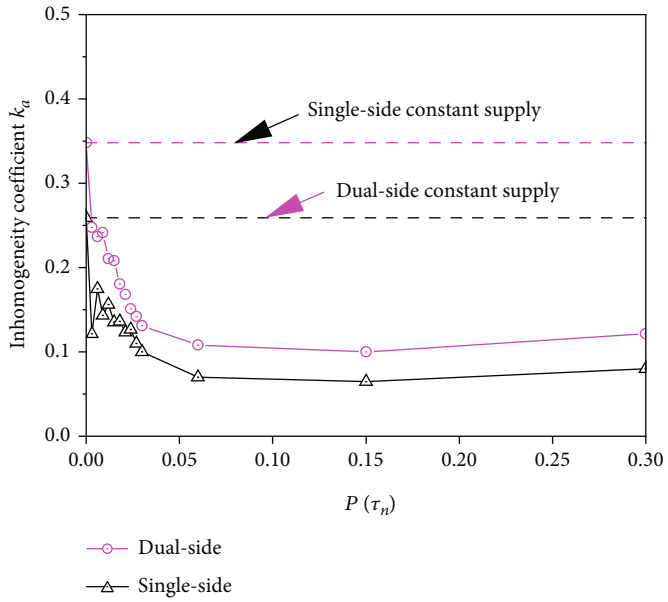

Figure 14: Inhomogeneity coefficient k_a with different time periods for single-side supply and dual-side supply bionic ventilation systems (square wave function).

employed to generate a set of sampling points that converge to the posterior distribution, and statistical analysis is performed to ascertain the statistical characteristics of the PPD.

In this paper, the Markov chain Monte Carlo (MCMC) method was utilized for sampling. The Markov chain was initialized at the center of the domain (4.5 m, 1.5 m) and subsequently underwent a burn-in period to converge to the vicinity of the actual source location.

The entire Markov chain has a length of 50,000. To ensure that it was fully mixed and the starting point is forgotten, the first half of the samples (30,000 iterations) were discarded, and the second half of the chain was used for inference. Samples from MCMC algorithms typically exhibit autocorrelation due to the inherent Markovian dependence structure. The degree of autocorrelation can be qualified using the autocorrelation function.

$$\rho_k = \frac{\mathrm{Cov}\left(M_i, M_{\mathrm{avg}}\right)}{\sqrt{\mathrm{Var}(M)}\sqrt{\mathrm{Var}\left(M_{\mathrm{avg}}\right)}} = \frac{\sum_{i=1}^{N-k}\left(M_i - M_{\mathrm{avg}}\right)\left(M_{i+k} - M_{\mathrm{avg}}\right)}{\sum_{i=1}^{N}\left(M_i - M_{\mathrm{avg}}\right)^2}. \tag{32}$$

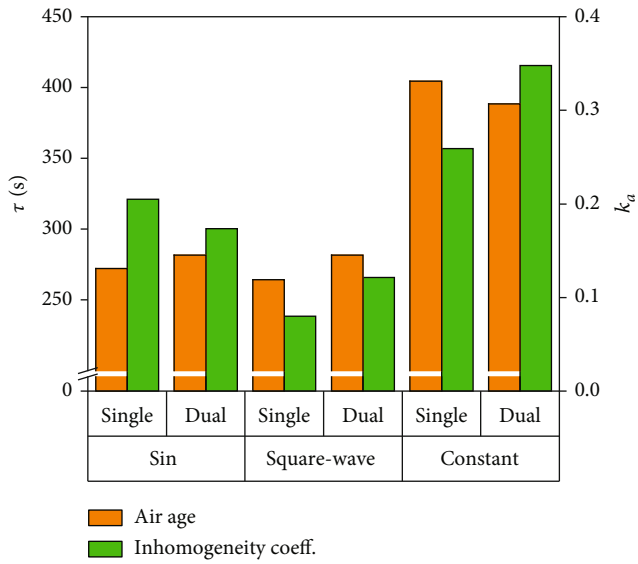

FIGURE 15: Air age and inhomogeneity coefficient comparison for single-side and dual-side supply bionic ventilation systems with different time-periodic functions.

By calculating the autocorrelation coefficient (defined by Equation (32)) between the accepted sampling points, it is possible to determine whether the Markov chain has reached convergence. Let M_i represent the sampling value at iteration step i. M_{avg} denotes the average sampling value, and N is the total iteration steps. Significant autocorrelation between samples indicated that the chain needs to be thinned, meaning that every interaction sample is taken to reduce the correlation before using the posterior statistics for inference. Figure 18 illustrates the degree of autocorrelation ρ_k as a function of the thinning interval in the Markov chain. From Figure 18, it can be observed that for the single-side ventilation system, the autocorrelation is small enough to conduct inference when the thinning interval is greater than 20, whereas for the dual-side ventilation system, the thinning interval needs to be at least 45 to obtain a sufficiently small autocorrelation. This means that suitable subsequences $\{X_k\}$, $\{Y_k\}$, and $\{S_k\}$ can be generated by MCMC sampling.

The next sampling point determined by the proposal distribution should be neither too far nor too close to the current point, and the acceptance rate can be adjusted to approximately 50% by continuously changing the hyperparameters, like standard deviation. Improved MCMC methods, such as Hamiltonian Monte Carlo [47], can also be employed to reduce the autocorrelation between consecutive sampling points.

The PPD of the source parameters, including the location and strength, are shown in Figure 19 using histogram plots. These plots provide a quantified representation of the marginal probability distribution of the source parameters. Based on Figure 19, the peaks of the histograms for both source position and intensity are located near the actual source parameters, as indicated by the red vertical line. The kernel density estimation (KDE) curves, represented by the blue lines, also exhibit peaks near the true values. These results demonstrate that Bayesian inference, coupled with the dynamic dual adjoint equation, effectively identifies sources in two types of bionic ventilation systems.

Table 2 presents the summary statistics of the source parameters generated from the MCMC samples for both single-side and dual-side ventilation cases. Compared to single-side ventilation, dual-side ventilation exhibits smaller standard deviation regions for both source location and intensity, suggesting a more concentrated posterior distribution. For the single-side bionic ventilation system, the distance between the KDE peak value and the true value of the x-coordinate is 0.2 m. However, the average difference is 1.0 m, and the standard deviation is 2.42 m, except for the KDE peak value, indicating a large error. This is due to the strong airflow organization in the domain near the vent, which results in a small concentration gradient in the horizontal direction and a relatively scattered distribution of sampling points. The KDE peak value of the y-coordinate of the pollution source is 0.1 m away from the true value, the average difference is 0.6 m, and the standard deviation is 0.44 m. The concentration gradient in the y-direction is relatively large, leading to more concentrated sampling results during the identification process. For the inverse identification of the source intensity, both the average value and the KDE peak value are closer to the true value, owing to the strong linear relationship between the measured pollutant concentrations at the sensors and the source intensity. For the dual-side bionic ventilation system, the high degree of matching of matching between the standard deviation and the KDE peak is attributed to source-2 being located in the recirculation zone, where the pollutants tend to change relatively smoothly.

During the sampling of the PPD, the acceptance and rejection of each sampling point in the x and y coordinates were recorded, as illustrated in Figure 20. The blue dots represent accepted sampling points, while the red dots represent rejected sampling points. The actual source location is marked by the yellow circle. The "saturation region" is represented by the blue area, and once the sampling points reach this area, the acceptance rate of the algorithm increases significantly. This indicates that the algorithm has reached the optimal parameter space that can be sampled from, and the Markov chain is in a convergent state. In Figure 20, the algorithm no longer accepts any values outside the blue range. In Figure 20(a), the distribution of accepted sampling points is concentrated in the upper left part of the computational domain, whereas in Figure 20(b), the distribution is concentrated in "stagnant zones," as shown in Figure 10(b). Therefore, the airflow organization of the flow field has a significant impact on the sampling space. The success of former identification results highlights the accuracy and reliability of the Bayesian inference method in identifying sources in bionic ventilation systems.

5.3. Discussion. In this study, the effectiveness and safety of bionic ventilation systems were investigated, with a focus on enhancing indoor air quality and identifying potential

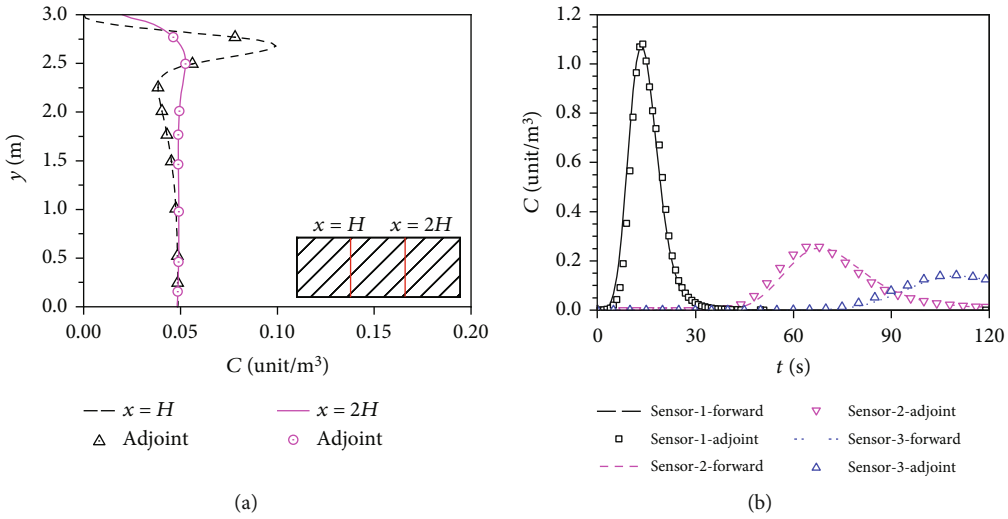

Figure 16: Comparison of space and temporal variation of concentration at three sensors using forward equation and dual adjoint equation. (a) Concentration comparison along two vertical lines after one time period. (b) Concentration comparison over one time period.

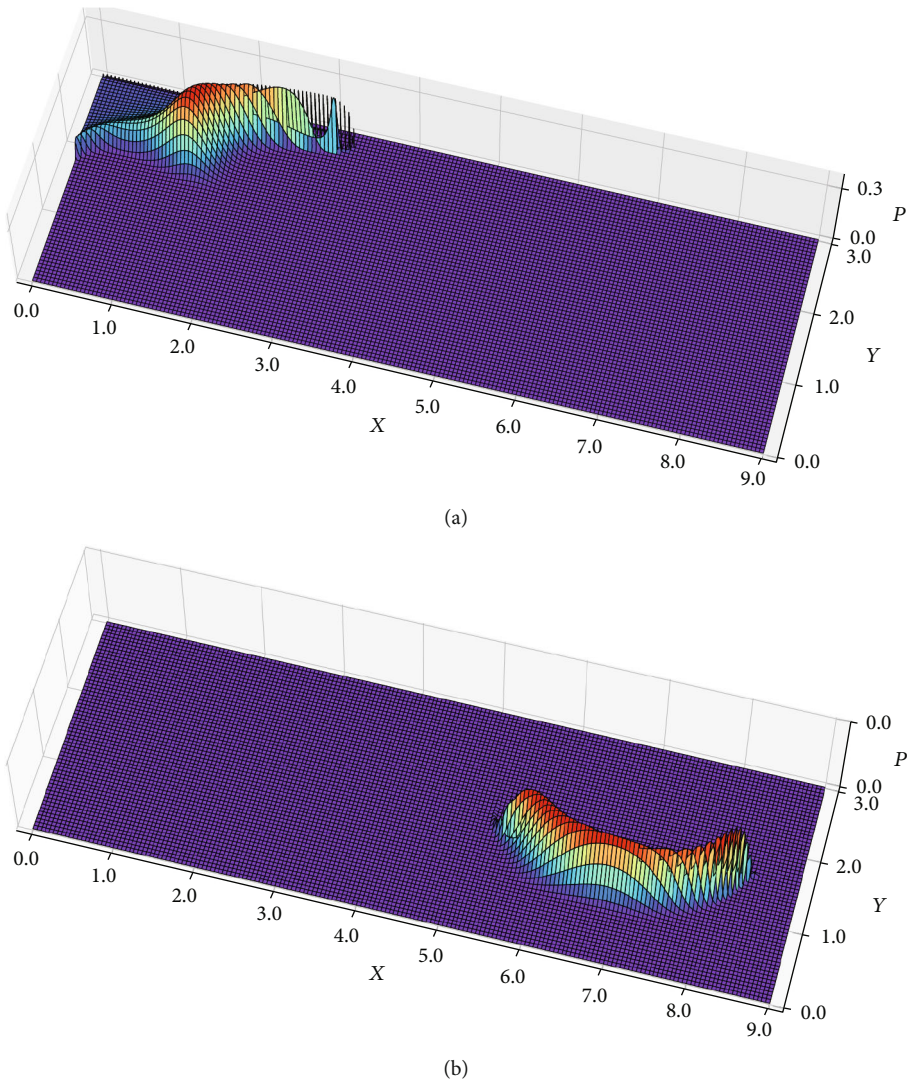

Figure 17: Posterior probability density function distribution of pollution source location. (a) Single-side ventilation with time-periodic supply (sine function, $T = 0.03\tau_n$). (b) Dual-side ventilation with time-periodic supply (sine function, $T = 0.03\tau_n$).

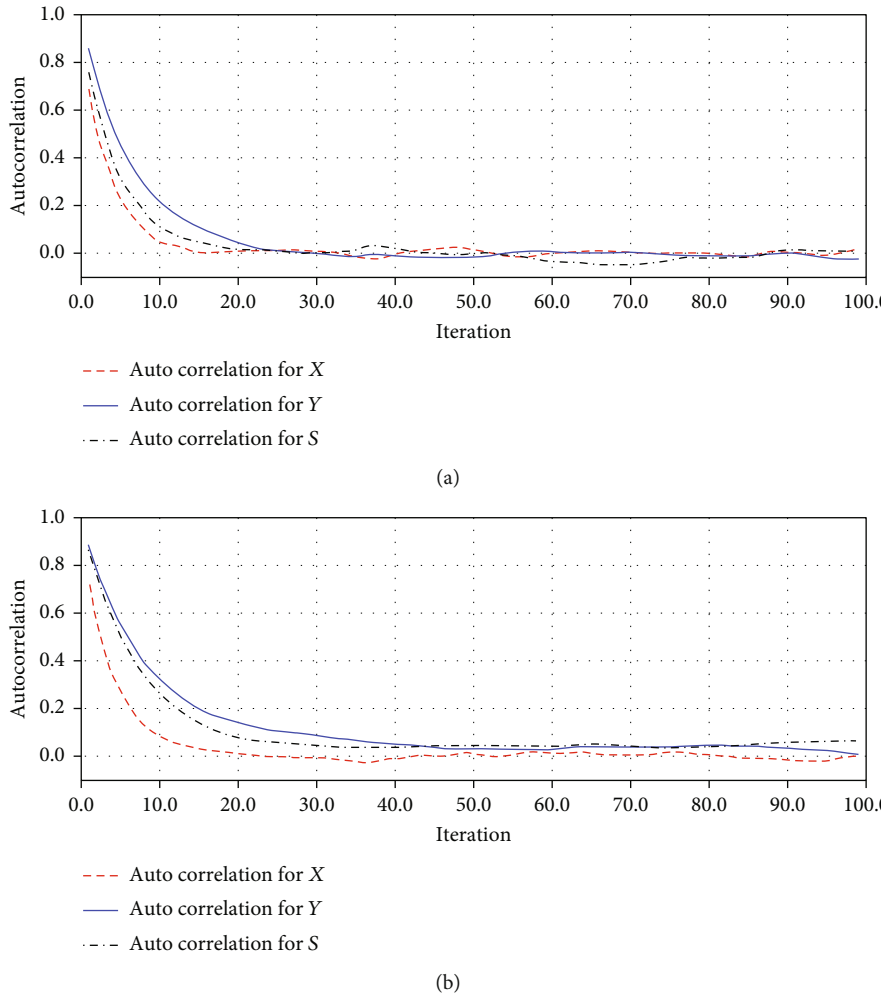

FIGURE 18: The autocorrelation plots for source parameter. (a) Single-side ventilation with time-periodic supply (sine function, $T = 0.03\tau_n$). (a) Dual-side ventilation with time-periodic supply (sine function, $T = 0.03\tau_n$).

pollution sources. The findings have significant implications for the design and implementation of bionic ventilation systems across various settings, such as residential, commercial, and public spaces.

Ventilation effectiveness, a key factor in maintaining a healthy and comfortable indoor environment, was evaluated. The results show that bionic ventilation systems, designed to create a more uniform air age distribution and minimize pollutants in stagnant zones, exhibit higher ventilation efficiency compared to traditional constant air-supply systems. A comparison between single-side and dual-side bionic ventilation systems revealed that both configurations lead to substantial improvements in ventilation effectiveness. The oscillatory flow in the enclosure, propelled by wall jets and the breakup of recirculation vortex rings, delivers fresh air to the middle of the room. The characteristics of the airflow organization formed by the bionic ventilation system can be observed in Figures 9 and 10. This mechanism effectively precludes the development of stagnant areas. By adjusting the supply air frequency of the bionic ventilation system to approach its natural frequency, ventilation efficiency can be improved. Such research is primarily focused on the field of heat exchange, rather than air quality. This topic will be explored in greater detail in future work.

Safety is another crucial aspect of the ventilation system. Accurate identification of pollution sources in indoor environments can be challenging due to the highly nonlinear nature of supply systems, particularly in dynamic flow fields. A Bayesian inference algorithm was employed in the paper to develop a methodology for identifying pollution sources in indoor environments under dynamic flow conditions. Through the combination of computational fluid dynamics (CFD) simulations and the Markov chain Monte Carlo (MCMC) sampling, it was demonstrated that indoor pollutant source parameters (including location and intensity) can be effectively identified with high confidence. Applying this method to real-world scenarios to explore its effectiveness and timeliness would be another worthwhile work of research. The quantity, placement, and accuracy of sensors play a significant role in the results of pollutant inverse identification. In this study, we employed only three sensors to identify source information, typically positioned near the

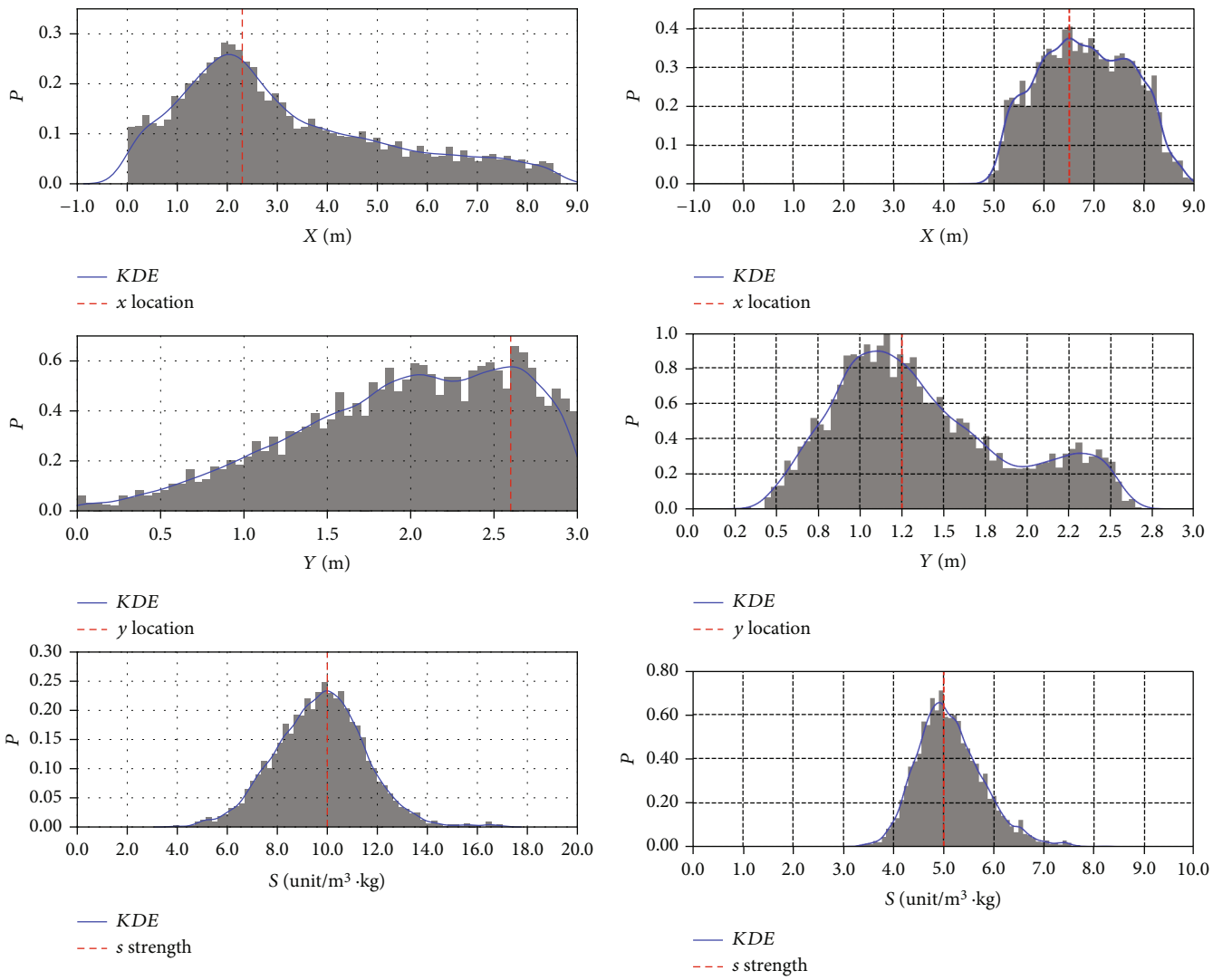

Figure 19: The histogram of source parameters estimation, with the actual value shown as the red vertical line. KDE is the kernel density function. (a) Single-side ventilation with time-periodic supply (sine function, $T = 0.03\tau_n$). (b) Dual-side ventilation with time-periodic supply (sine function, $T = 0.03\tau_n$).

Table 2: True values of the source parameters and the summary of the estimation results.

Type	True value		Source location estimation			Source rate estimation		
	(x, y)[a]	S[b]	KDE[c] peak value	Average value	Standard deviation	KDE peak value	Average value	Standard deviation
Single-side	(2.3, 2.6)	10.0	(2.1, 2.7)	(3.1, 2.0)	(2.42, 0.44)	10.0	9.7	3.22
Dual-side	(6.5, 1.2)	5.0	(6.5, 1.1)	(6.8, 1.2)	(0.69, 0.17)	4.9	10.2	0.74

[a]Unit of the source location is m. [b]Unit of the source location is mL/s. [c]Kernel density estimation, used to estimate unknown PDF.

ceiling, floor, and side walls, which highlights the efficiency of the algorithm. While increasing the number of sensors can certainly improve identification accuracy, it also comes with additional layout costs. The influence of a sensor's quantity, placement, and accuracy on the results of pollutant inverse identification will be the focus of future research.

In conclusion, the findings highlight the potential of bionic ventilation systems in enhancing ventilation effectiveness and safety simultaneously in indoor environment. By accurately and efficiently identifying pollution sources, these systems can play an essential role in maintaining healthy and comfortable living and working spaces.

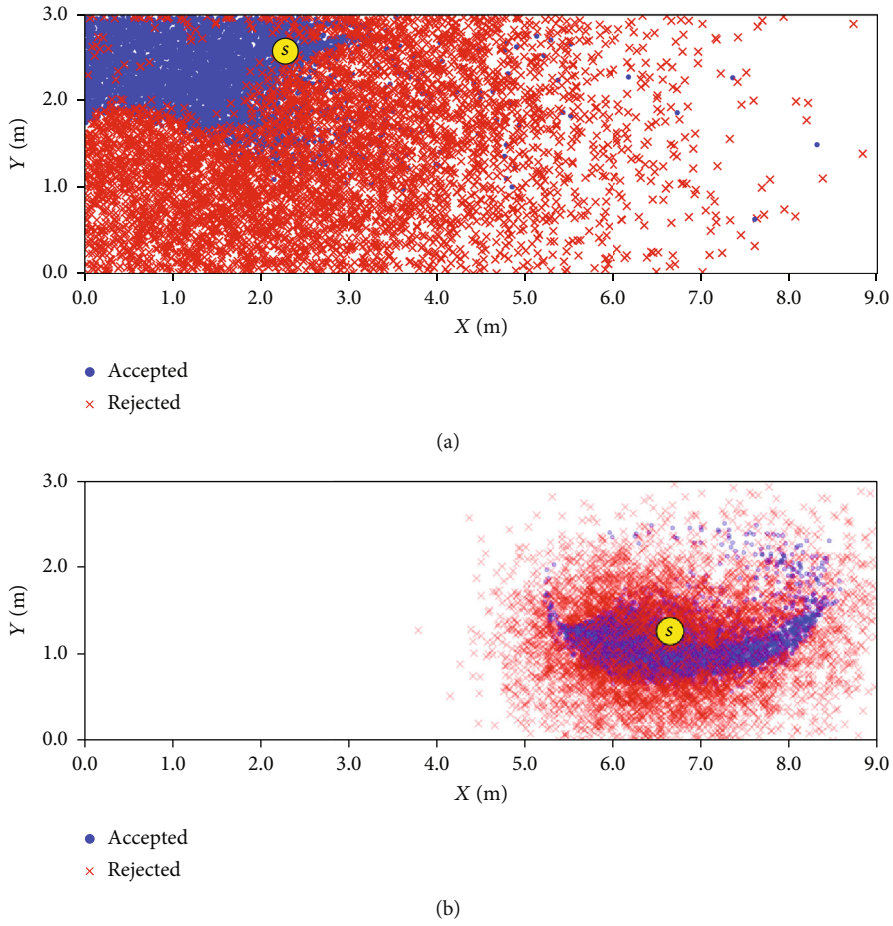

FIGURE 20: Source location estimation sampling point distribution. (a) Single-side ventilation with time-periodic supply (sine function, $T = 0.03\tau_n$). (b) Dual-side ventilation with time-periodic supply (sine function, $T = 0.03\tau_n$).

6. Conclusions and Limitations

This article has proposed a new type of ventilation system, namely, bionic ventilation systems, which are aimed at generating a more uniform mean velocity distribution, reducing pollutants inside stagnant zones, and achieving higher ventilation efficiency simultaneously. The performance of two bionic ventilation systems, single-side and dual-side ventilations, was compared with a traditional constant air-supply system. In this context, the constant air-supply system denotes an air supply with a consistent airflow rate, as opposed to the bionic ventilation system which employs periodic airflow rates. Our results showed that the bionic ventilation systems had higher ventilation efficiency and lower inhomogeneity coefficient of pollutants. Furthermore, bionic ventilation systems with different time periods of sine and rectangular wave functions were compared. The turning point occurs at a period of $0.06\tau_n$, where the ventilation efficiency increases rapidly as the period increases below this point, whereas, beyond this critical point, promotion of the period has little effect on ventilation efficiency. The present research further demonstrated that the rectangular wave function could be an effective alternative to the sine wave function in cases where it is difficult to produce sinusoidal time-periodic ventilation.

Accurately identifying pollution sources in the bionic ventilation system poses significant challenges, primarily due to the highly nonlinear nature of the supply system, especially when attempting to identify those pollution sources in dynamic flow fields. Bayesian inference algorithm has been used to develop a methodology for identifying pollution sources in indoor environments under dynamic flow fields. Factors that influence the accuracy of source identification were also discussed in detail.

By combining the CFD method to solve the dual adjoint equation and Bayesian inference using MCMC sampling, the parameters of indoor pollutant sources (including the location and intensity of the source) can be identified in a short time with high confidence. From the results, the peaks of the KDE distributions and the sampling average values of the source location and intensity are all consistent with the actual source parameters. The largest deviation for the KDE peak location is less than 0.2 m with a relative error of 8%, while the KDE peak for the source intensity deviation is 0.3 mL/s with a relative error of 3%. This demonstrates the effectiveness and reliability of the method for source identification in bionic ventilation systems with strong instability and nonlinearity characteristics.

In this paper, it is assumed that the model and monitoring errors follow a Gaussian distribution. When there are

monitoring singularities, the Laplace distribution can be used to improve the accuracy of the sampling estimation. When the observation error is extremely small and can be considered negligible, the likelihood function can be represented using the Dirac delta function. Only three monitoring points are used in the calculation domain, which may result in an overly large posterior distribution or multiple solutions with limited "evidence." It can be foreseen that increasing the number of pollutant monitoring points can effectively improve the accuracy of inversion identification. Additionally, the placement of monitoring points has a significant impact on the posterior distribution of pollutants. In the absence of prior information about the location of the pollutant source, it is still valuable to explore effective arrangements of monitoring points. The effectiveness of the proposed method may be influenced by the complexity of the indoor environment, the accuracy of the CFD simulations, and the quality of the monitoring data. All sensors have inherent detection thresholds and strategic errors. As a result, the methods for effectively collecting pollutant source data, along with the accuracy and efficacy of the algorithm, warrant further analysis and investigation. In practice, the source-measurement relationship can be precalculated for a specific room under a determined airflow organization (steady/unsteady). When the pollutant source release position is fixed, the pollutant concentration distribution within the computational domain and the concentration values at the receptors form a linear system. Any source release intensity can be obtained by linear scaling of this system. These factors should be carefully considered when applying the method in real-world scenarios.

Data Availability

The data used to support the findings of this study are available from the corresponding author upon request.

Additional Points

Highlights. Novel bionic ventilation system was proposed to achieve effectiveness and safeness. Source term estimation method suitable for unsteady flow fields was established. Two kinds of bionic systems, single-single and dual-side ventilations, were compared. Time-periodic supply with different functions and periods were compared. Proposed bionic ventilation system was demonstrated for future engineering applications.

Conflicts of Interest

The authors declare that they have no conflicts of interest.

Authors' Contributions

Hong-Liang Zhang was responsible for the conceptualization, methodology, and writing—original draft. Bing Li was responsible for the data analysis. Jin Shang was responsible for the mathematical calculations. Wei-Wei Wang was responsible for the data correlation and expression. Fu-Yun Zhao was responsible for the supervision, methodology, and submission.

Acknowledgments

Authors would gratefully acknowledge the financial support of the National Key R&D Program of China (No. 2022YFC3801600); the Science Foundation (Meteorology) Innovation Development Joint Fund Key Project of Hubei Province (Grant No. 2023M15); the Foreign Aid Project for High-Level Cooperation and Exchange Activities of the Ministry of Science and Technology of China (Grant No. 202213); the Wuhan University Specific Fund for Major School-Level Internationalization Initiatives (Grant No. WHU-GJZDZX-PT08, Wuhan University); the Provincial Key R&D Program of Hunan (Grant No. 2022SK2084, Hunan University of Technology); the Natural Science Foundation of China (NSFC) (Grant No. 51778504 and Grant No. U1867221).

References

[1] C. Mattiuzzi and G. Lippi, "Cancer statistics: a comparison between world health organization (WHO) and global burden of disease (GBD)," *European Journal of Public Health*, vol. 30, no. 5, pp. 1026-1027, 2020.

[2] Y. M. Kim, S. Harrad, and R. M. Harrison, "Concentrations and sources of VOCs in urban domestic and public microenvironments," *Environmental Science & Technology*, vol. 35, no. 6, pp. 997–1004, 2001.

[3] F.-Y. Zhao, G. Shen, K.-J. Liu, Y. Xu, D. Liu, and H. Q. Wang, "Room airborne pollutant separation by the use of air curtains in the large building enclosure: infiltration efficiency and partial enclosure ventilation rate," *Journal of Building Engineering*, vol. 18, pp. 386–394, 2018.

[4] D.-D. Zhang, Y. Cai, D. Liu, F. Y. Zhao, and Y. Li, "Dual steady flow solutions of heat and pollutant removal from a slot ventilated welding enclosure containing a bottom heating source," *International Journal of Heat and Mass Transfer*, vol. 132, pp. 11–24, 2019.

[5] Q. Chen, Z. Zhai, X. You, and T. Zhang, *Inverse Design Methods for the Built Environment*, Routledge, 2017.

[6] S. Gilani, H. Montazeri, and B. Blocken, "CFD simulation of stratified indoor environment in displacement ventilation: validation and sensitivity analysis," *Building and Environment*, vol. 95, pp. 299–313, 2016.

[7] X. Ye, H. Zhu, Y. Kang, and K. Zhong, "Heating energy consumption of impinging jet ventilation and mixing ventilation in large-height spaces: a comparison study," *Energy and Buildings*, vol. 130, pp. 697–708, 2016.

[8] T. Karimipanah and H. B. Awbi, "Theoretical and experimental investigation of impinging jet ventilation and comparison with wall displacement ventilation," *Building and Environment*, vol. 37, no. 12, pp. 1329–1342, 2002.

[9] Z. Lin, T. T. Chow, C. F. Tsang, K. F. Fong, and L. S. Chan, "Stratum ventilation - a potential solution to elevated indoor temperatures," *Building and Environment*, vol. 44, no. 11, pp. 2256–2269, 2009.

[10] L. Tian, Z. Lin, and Q. Wang, "Experimental investigation of thermal and ventilation performances of stratum ventilation," *Building and Environment*, vol. 46, no. 6, pp. 1309–1320, 2011.

[11] A. K. Melikov, R. Cermak, and M. Majer, "Personalized ventilation: evaluation of different air terminal devices," *Energy and Buildings*, vol. 34, no. 8, pp. 829–836, 2002.

[12] G. Cao, H. Awbi, R. Yao et al., "A review of the performance of different ventilation and airflow distribution systems in buildings," *Building and Environment*, vol. 73, pp. 171–186, 2014.

[13] L. D. Prockop and R. I. Chichkova, "Carbon monoxide intoxication: an updated review," *Journal of the Neurological Sciences*, vol. 262, no. 1-2, pp. 122–130, 2007.

[14] R. E. Brown, J. D. Brain, and N. Wang, "The avian respiratory system: a unique model for studies of respiratory toxicosis and for monitoring air quality," *Environmental Health Perspectives*, vol. 105, no. 2, pp. 188–200, 1997.

[15] C. Kandzia, M. Schmidt, and D. Miller, "Room airflow effects applying unsteady boundary conditions," in *The 12th International Conference on Air Distribution in Rooms*, pp. 132–140, Trondheim, Norway, 2011.

[16] A. Sattari, B. Fallenius, J. Fransson, and M. Sandberg, "PIV visualization study in a two-dimensional room model with rapid time varying ventilation flow rates," in *The 12th International Conference on Air Distribution in Rooms*, pp. 970–980, Trondheim, Norway, 2011.

[17] T. Van Hooff and B. Blocken, "Mixing ventilation driven by two oppositely located supply jets with a time-periodic supply velocity: a numerical analysis using computational fluid dynamics," *Indoor and Built Environment*, vol. 29, no. 4, pp. 603–620, 2020.

[18] S. Kaam, P. Raftery, H. Cheng, and G. Paliaga, "Time-averaged ventilation for optimized control of variable-air-volume systems," *Energy and Buildings*, vol. 139, pp. 465–475, 2017.

[19] T. R. Nielsen and C. Drivsholm, "Energy efficient demand controlled ventilation in single family houses," *Energy and Buildings*, vol. 42, no. 11, pp. 1995–1998, 2010.

[20] T. Pham, L. J. Brochard, and A. S. Slutsky, "Mechanical ventilation: state of the art," *Mayo Clinic Proceedings*, vol. 92, no. 9, pp. 1382–1400, 2017.

[21] D. Liu, F.-Y. Zhao, H.-X. Yang, J. Chen, and C. Ye, "Probability adjoint identification of airborne pollutant sources depending on one sensor in a ventilated enclosure with conjugate heat and species transports," *International Journal of Heat and Mass Transfer*, vol. 102, pp. 919–933, 2016.

[22] X. Liu and Z. Zhai, "Inverse modeling methods for indoor airborne pollutant tracking: literature review and fundamentals," *Indoor Air*, vol. 17, no. 6, pp. 419–438, 2007.

[23] M. Hutchinson, H. Oh, and W. H. Chen, "A review of source term estimation methods for atmospheric dispersion events using static or mobile sensors," *Information Fusion*, vol. 36, pp. 130–148, 2017.

[24] M. Amirabdollahian and B. Datta, "Identification of contaminant source characteristics and monitoring network design in groundwater aquifers: an overview," *Journal of Environmental Protection*, vol. 4, no. 5, pp. 26–41, 2013.

[25] F. Xue, X. Li, and W. Zhang, "Bayesian identification of a single tracer source in an urban-like environment using a deterministic approach," *Atmospheric Environment*, vol. 164, pp. 128–138, 2017.

[26] A. Keats, E. Yee, and F. S. Lien, "Bayesian inference for source determination with applications to a complex urban environment," *Atmospheric Environment*, vol. 41, no. 3, pp. 465–479, 2007.

[27] F. Wang, X. Zhou, J. Huang, H. Wang, H. Kikumoto, and C. Deng, "Natural gas leakage estimation in underground utility tunnels using Bayesian inference based on flow fields with gas jet disturbance," *Process Safety and Environmental Protection*, vol. 165, pp. 532–544, 2022.

[28] X. Yan, W. Dong, Y. An, and W. Lu, "A Bayesian-based integrated approach for identifying groundwater contamination sources," *Journal of Hydrology*, vol. 579, p. 124160, 2019.

[29] D. Gamerman and H. F. Lopes, *Markov Chain Monte Carlo: Stochastic Simulation for Bayesian Inference*, CRC Press, 2006.

[30] K. Beven and J. Freer, "Equifinality, data assimilation, and uncertainty estimation in mechanistic modelling of complex environmental systems using the GLUE methodology," *Journal of Hydrology*, vol. 249, no. 1-4, pp. 11–29, 2001.

[31] M. Giles, N. Pierce, M. Giles, and N. Pierce, "Adjoint equations in CFD-duality, boundary conditions and solution behavior," in *13th Computational Fluid Dynamics Conference*, p. 1850, Snowmass Village, CO, USA, 1997.

[32] G. I. Marchuk, *Adjoint Equations and Analysis of Complex Systems*, Springer Science & Business Media, 1995.

[33] P. V. Nielsen, L. Rong, and I. O. Cortes, "The IEA annex 20 two-dimensional benchmark test for CFD predictions," in *10th Rehva World Congress: Sustainable Energy Use in Buildings*, pp. 9–12, Antalya, Turkey, 2010.

[34] D. Li, C. C. Menassa, and V. R. Kamat, "Personalized human comfort in indoor building environments under diverse conditioning modes," *Building and Environment*, vol. 126, pp. 304–317, 2017.

[35] W. Rodi, *Turbulence Models and Their Application in Hydraulics*, CRC Press, 1993.

[36] C. G. Popovici, "Hvac system functionality simulation using ANSYS-Fluent," *Energy Procedia*, vol. 112, pp. 360–365, 2017.

[37] M. Cortés, P. Fazio, J. Rao, W. Bustamante, and S. Vera, "Modelación CFD de casos básicos de convección en ambientes cerrados: Necesidades de principiantes en CFD para adquirir habilidades y confianza en la modelación CFD," *Revista de Ingeniería de Construcción (RIC)*, vol. 29, no. 1, pp. 22–45, 2014.

[38] E. Lim, M. Sandberg, and K. Ito, "Returning characteristics of pollutants for a local domain in the presence of returning and recirculating airflow in indoor environments," *Indoor Air*, vol. 31, no. 4, pp. 1267–1280, 2021.

[39] J. Le Dréau, P. Heiselberg, and P. V. Nielsen, *Simulation with Different Turbulence Models in an Annex 20 Benchmark Test Using Star-CCM+*, Aalborg University, Department of Civil Engineering, 2012.

[40] M. Weng, P. V. Nielsen, and L. Liu, *A Discussion of Low Reynolds Number Flow for the Two-Dimensional Benchmark Test Case*, Aalborg University, Department of Civil Engineering, 2012.

[41] K. Ito, K. Inthavong, T. Kurabuchi et al., "CFD benchmark tests for indoor environmental problems: part 1 isothermal/non-isothermal flow in 2D and 3D room model," *International Journal of Architectural Engineering Technology*, vol. 2, no. 1, pp. 1–22, 2015.

[42] N. Ivanov, M. Zasimova, E. Smirnov, and D. Markov, "Evaluation of mean velocity and mean speed for test ventilated room from RANS and LES CFD modeling," *EDP Sciences*, vol. 85, article 02004, 2019.

[43] M. Sandberg, "What is ventilation efficiency?," *Building and Environment*, vol. 16, no. 2, pp. 123–135, 1981.

[44] X. Li, H. Cai, R. Li, Y. Zhao, X. Ma, and X. Shao, "A theoretical model to calculate the distribution of air age in general ventilation system," *Building Services Engineering Research and Technology*, vol. 33, no. 2, pp. 159–180, 2012.

[45] T.-F. Zhang and Q. Chen, "Identification of contaminant sources in enclosed environments by inverse CFD modeling," *Indoor Air*, vol. 17, no. 3, pp. 167–177, 2007.

[46] O. Martin, *Bayesian Analysis with Python*, Packet Publishing Ltd, 2016.

[47] M. Girolami and B. Calderhead, "Riemann manifold Langevin and Hamiltonian Monte Carlo methods," *Journal of the Royal Statistical Society: Series B (Statistical Methodology)*, vol. 73, no. 2, pp. 123–214, 2011.